

ADVANCES IN RADIATION TRANSPORT MODELING USING
LATTICE BOLTZMANN METHODS

by

Richard McCulloch

B.S., Utah State University, 2013

A THESIS

submitted in partial fulfillment of the
requirements for the degree

MASTER OF SCIENCE

Mechanical and Nuclear Engineering
College of Engineering

KANSAS STATE UNIVERSITY
Manhattan, Kansas

2015

Approved by:

Major Professor
Hitesh Bindra

Copyright

Richard McCulloch

2015

Abstract

This thesis extends the application of Lattice Boltzmann Methods (LBM) to radiation transport problems in thermal sciences and nuclear engineering. LBM is used to solve the linear Boltzmann transport equation through discretization into Lattice Boltzmann Equations (LBE). The application of weighted summations for the scattering integral as set forth by Bindra and Patil¹ are used in this work. Simplicity and localized discretization are the main advantages of using LBM with fixed lattice configurations for radiation transport problems. Coupled solutions to radiation transport and material energy transport are obtained using a single framework LBM.

The resulting radiation field of a one dimensional participating and conducting media are in very good agreement with benchmark results using spherical harmonics, the P_1 method. Grid convergence studies were performed for this coupled conduction-radiation problem and results are found to be first-order accurate in space. In two dimensions, angular discretization for LBM is extended to higher resolution schemes such as D_2Q_8 and a generic formulation is adopted to derive the weights for Radiation Transport Equations (RTEs). Radiation transport in a two dimensional media is solved with LBM and the results are compared to those obtained from the commercial software COMSOL, which uses the Discrete Ordinates Method (DOM) with different angular resolution schemes. Results obtained from different lattice Boltzmann configurations such as D_2Q_4 and D_2Q_8 are compared with DOM and are found to be in good agreement. The verified LBM based radiation transport models are extended for their application into coupled multi-physics problems. A porous radiative burner is modeled as a homogeneous media with an analytical velocity field. Coupling is performed between the convection-diffusion energy transport equation with the analytical

velocity field. Results show that radiative transport heats the participating media prior to its entering into the combustion chamber.

The limitations of homogeneous models led to the development of a fully coupled LBM multi-physics model for a heterogeneous porous media. This multi-physics code solves three physics: fluid flow, conduction-convection and radiation transport in a single framework.

The LBE models in one dimension are applied to solve one-group and two-group eigenvalue problems in bare and reflected slab geometries. The results are compared with existing criticality benchmark reports for different problems. It is found that results agree with benchmark reports for thick slabs (>4 mfp) but they tend to disagree when the critical slab dimensions are less than 3 mfp. The reason for this disagreement can be attributed to having only two angular directions in the one dimensional problems.

Table of Contents

List of Figures	viii
List of Tables	xi
Acknowledgements	xi
Dedication	xii
1 Introduction	1
1.1 Radiation Transport in Matter	1
1.2 Background and History of LBM	3
1.2.1 Lattice Gas Automata	3
1.2.2 LBM Lattice Configurations	5
1.2.3 Benefits and Drawbacks of LGA	7
1.2.4 LBM from LGA	7
1.3 Boundary Conditions for LBM	8
1.4 Directions and Weight Factors	10
1.5 Radiative Transport LBE	14
2 One Dimensional Multiple-Mode Heat Transfer	17
2.1 Introduction	17
2.2 Mathematical Formulation	18
2.3 Numerical Examples	19
2.3.1 Radiation: Su-Olson Wave	19

2.3.2	Radiation-Conduction: One Dimensional Media	22
2.4	Conclusions	26
3	Two Dimensional Multiple-Mode Heat Transfer	28
3.1	Introduction	28
3.2	Radiative Validation	28
3.3	Convection-Radiation: Homogeneous Radiative Porous Burner	32
3.4	Radiation-Convection: Heterogeneous Radiative Porous Burner	37
3.5	Conclusions	41
4	Nuclear Reactor Criticality	43
4.1	Chain Reaction	43
4.2	Neutron Transport Equation	44
4.2.1	Rate of Change	44
4.2.2	Gains	45
4.2.3	Losses	46
4.2.4	Neutron Balance	47
4.3	Reactor Criticality	48
4.3.1	Operating Conditions	48
4.3.2	Eigenvalue Problem	49
4.4	Boundary Conditions	50
4.4.1	Vacuum Boundary Conditions	50
4.4.2	Reflected Boundary Conditions	51
4.4.3	Periodic Boundary Conditions	52
4.5	Criticality Condition	52
4.5.1	Lattice Boltzmann Equation	52

4.5.2	P_1 Method	53
4.5.3	Power Iteration Method	54
4.6	Benchmark Problems	56
4.6.1	One Group Bare Reactor	57
4.6.2	One Group Reflected Reactor	58
4.6.3	One Group Reactor with Cladding and Moderator	58
4.6.4	Two Group Bare Reactor	58
4.6.5	Two Group Reflected Reactor	60
4.6.6	Two Group Infinite Slab Lattice Cell Reactor	60
4.7	Conclusions	64
5	Conclusions and Future Work	65
5.1	Conclusions	65
5.2	Future Work	67
	Bibliography	69
A	Example Codes	74
A.1	2D LBM Code	74
A.2	1D Criticality Code	79
A.3	4 Region Critical Reactor	80

List of Figures

1.1	One dimensional LBM lattice configuration.	6
1.2	Various two and three dimensional LBM lattice configurations showing (a) D_2Q_5 , (b) D_2Q_9 , (c) D_3Q_7 , and (d) D_3Q_{19} lattices.	6
1.3	Distances traveled in each direction in a single time step using a) LBM and b) DOM methods.	11
2.1	Su-Olson results for the case of $\kappa_a = 1$, $\sigma_s = 0$, $\nu = 1$, $x_o = 0.5$, $\rho = 1$ and $t_o = 10$	21
2.2	Temperature profile with varying optical thicknesses. $\theta_L = 1$, $\theta_R = 0.5$, $\tau_L = \kappa_a L = 1$ and (a) $\varepsilon_0 = \varepsilon_2 = 0$ (b) $\varepsilon_1 = \varepsilon_2 = 1$	25
2.3	Temperature profile with varying optical thicknesses. $N = 0.01$, $\theta_L = 1$, $\theta_R = 0.5$ and $\tau_L = \kappa_a L = 1$	25
2.4	Error as a function of node spacing for the participating slab example. The slope of the log of the error follows a 1:1 ratio with Δx , thus the method is observed to be first order accurate.	26
3.1	Radiative intensity profile along the coordinate $\tau_y = 0.5$ with $\sigma_s = 1$ for (a) D_2Q_4 versus DOM S_2 and (b) D_2Q_8 versus DOM S_4 . $\theta_{wall} = 0$ and $\theta_m = 1$	30
3.2	Radiative intensity field for $\sigma_s = 1$, $\theta_{wall} = 0$ and $\theta_m = 1$. Maximum absolute relative errors between the profiles are $\varepsilon = 0.0045$, $\varepsilon = 0.0024$ and $\varepsilon = 0.0217$ for $\kappa = 0.01$, $\kappa = 1$ and $\kappa = 10$, respectively.	31
3.3	Geometry for the case of a homogeneous porous burner.	36

3.4	Temperature distribution for the case of a non-participating homogeneous porous media, i.e. without any radiation absorption in the domain.	36
3.5	Temperature distribution for the case of a participating homogeneous porous media, i.e. with radiation absorption in the domain.	37
3.6	Heterogeneous porous burner with large flow obstacles with different material properties. Size, aspect ratio and grid size are chosen to be exactly the same as the homogeneous case.	37
3.7	Velocity field for flow around the obstacles inside the porous burner, solved with LBM. Colors correspond to the non-dimensional velocity magnitude along the streamline.	39
3.8	Temperature contour for the entire two dimensional domain with radiatively transparent obstacles ($\beta = 0$).	40
3.9	Temperature contour for the entire two dimensional domain with radiatively opaque obstacles ($\beta = 2$ and $N = 0.001$).	40
4.1	A two dimensional domain with (a) vacuum (b) reflected and (c) periodic boundary conditions on a single surface.	51
4.2	Algorithm for the power iteration method.	55
4.3	Normalized flux profile for the one-group ^{235}U (b) reactor with iron cladding and a sodium moderator using LBM and diffusion theory, both with Mark boundary conditions	59
4.4	Normalized flux profile for the two-group bare research reactor composed of ^{235}U (c).	61
4.5	Normalized flux profile for the two-group infinite slab lattice cell ^{235}U reactor with $r_c = 2.719087$ cm and $t_r = 7.510225$ cm for both P_1 and LBM methods.	62
A.1	Radiative field strength throughout the medium.	75

A.2 Radiative field strength along the centerline $y = 0.5$	75
A.3 Slab geometry for the non-symmetric monoenergetic 4 region reactor with cladding and a moderator	80

List of Tables

1.1	Directional weights for one dimensional and two dimensional lattices used in radiative simulations.	13
4.1	One-group macroscopic cross sections.	57
4.2	Two-group macroscopic cross sections.	60
A.1	One-group macroscopic cross sections for the 4 region reactor	80

Acknowledgments

I would like to thank my advisor, Hitesh Bindra, for his constant friendly encouragement and involvement in my research. I am especially grateful that Dr. Bindra saw potential in me and gave me the opportunity to work with him on these Lattice Boltzmann Method applications.

I am also very thankful for the work done by exceptionally gifted minds, which work provided a solid foundation for my research. A few specific people are Pietro Asinari and Subhash Mishra for their pioneering efforts in the application of LBM to heat transfer. For your work I am grateful and I echo the words of Sir Isaac Newton, “*If I have seen further than others, it is by standing upon the shoulders of giants.*”

I would like to thank Brian Yurk for introducing me to L^AT_EX as a freshman while taking Calculus I, and for fostering in me a deep appreciation for the application of mathematics. I am very grateful for the Detexify application,² thought up and created by Philipp Kühn and Daniel Kirsch. Invaluable time was spent on research instead of looking up symbols thanks to Detexify.

Dedication

I would like to dedicate this work to my family. My parents, Lonnie and Jeanette, taught me the value of education by their examples. They taught me that whatever goal I have I can attain with sufficient effort.

I also want to thank my beautiful wife, Kendra, for the love and support she has given me through our entire journey up to this point. My life will forever be enriched by her example. I am especially grateful for her courage and strength in raising our 5 amazing children, Mason, Logan, Cayden, Cadia and Callie, while I have been at study groups, teaching classes, attending classes or working late on research.

Special thanks go to my brothers and sisters, Josef, Tiffany, Ashley, Joshua and Seth, for their continued support. I would not be the person I am today without their encouragement and examples.

Chapter 1

Introduction

1.1 Radiation Transport in Matter

As radiation travels through a material medium, there are multiple mechanisms through which it can interact with that medium. Neutral particles can collide with nuclei, causing various possible reactions. Charged particles such as electrons and protons can interact with the negatively charged electron cloud or the positively charged nucleus, thus depositing energy in the medium. Volumetric transport of radiation is a critically important factor in many applications ranging from production of wide-bandgap semiconductor materials³ and ceramic sensors⁴ to performance of combustion chambers⁵. The transport mechanisms in nuclear reactors⁶, isotope production⁷ and radiation detector equipment⁸ are a few more examples with specific applications to nuclear technology. With the growing interest in high temperature systems for nuclear and other energy sources, the role of radiation transport in the design and analysis of such systems is expected to play an important role.

Thermal engineering problems involving radiation transport are traditionally classified into two categories - systems where surface to surface thermal exchange is quantified using the Stefan-Boltzmann law, and other problems where radiation transport through the participating media should be quantified. For processes such as glass making, the radiation profile

in the media becomes a crucial design factor.⁹ Solving for the radiative transport throughout the media is computationally expensive compared to using the Stefan-Boltzmann law, however the results give more information about the physics going on inside the media.

Various methods have been developed to solve the radiation transport equation (RTE). Radiation transport problems require the full solution of the RTE. Some of the popular methods to solve the RTE include the Finite Volume Method, Discrete Ordinate Method (DOM), Spherical Harmonics, Discrete Transfer Method, Collapsed Dimension Method, Probability Method and Method of Characteristics. The aforementioned methods reduce the domain for radiation by making various assumptions. The typical approach is to discretize the angular space in order to represent the entire domain. For stochastic radiation transport the geometry is often simplified and directions are sampled from a probability distribution.

The Lattice Boltzmann Method (LBM) is a deterministic computational method based on the cellular gas automata models, discussed later, via a system of lattice Boltzmann equations (LBE). As will be discussed later in this chapter, LBM implements inter-particle collisions to simulate physical phenomenon such as fluid motion. The velocity of each particle is governed by a particle distribution function, although sampling is systematic, making LBM a deterministic algorithm. Time advances in finite steps, during which collision rules are applied such that the governing physics are not violated.

A new approach was proposed by Asinari et al. for radiative transport simulations by using the LBM¹⁰ for modeling radiative heat transfer in the participating media. In 2011 Ma et. al.¹¹ re-derived LBE's for radiation transport using Chapman-Enskog expansion. They solved for the steady-state radiative profile between gray plates in a non-scattering media and found good agreement between the LBM results and the analytical profile. In 2012 Bindra and Patil¹ applied LBM to one and two dimensional steady-state radiative and neutron transport problems with isotropic and anisotropic scattering medias. Results were found to be very agreeable with spherical harmonics and DOM solutions. Some of these example studies¹⁰ showed that LBM used as little as 14% of CPU time as compared to the

finite volume method for a one dimensional problem. The application of LBM to radiative problems makes it a prime candidate for an inherently coupled multiphysics solver, where radiative transport and material (e.g. fluid) transport can be solved in a single framework.

1.2 Background and History of LBM

LBM is a mesoscopic method in which groups of particles represent the properties of a material as an ensemble average of the individual particles. To better understand the modeling scale of LBM it would be helpful to take a brief look at the application of LBM to fluid mechanics.

LBM uses statistical mechanics to represent the motion of particles. It was developed from the Lattice Gas Automata (LGA) model which is a microscopic method, enforcing the physics for each atom. The remainder of Sec. 1.2 gives a background of LGA and shows how LBM was developed to overcome various problems facing the LGA model.

1.2.1 Lattice Gas Automata

LGA is an artificial microscopic method that was developed to describe gas kinetics. The first known LGA model was the HPP model,¹² which separates the movement of particles into two steps: collision and streaming. In the collision step local physics are enforced and in the streaming step the numerical results are propagated in 4 cardinal directions, referred to as streaming directions.

The HPP collision step enforces a boolean quantity at a particular node. In essence a particle either exists at a specific node, or it does not. Mathematically the collision operation is given by Eq. 1.1, where $n=0$ or 1 and is the number of particles, x is the node location, t is the time, and Λ_i is the collision operator for the i^{th} direction and is given in Eq. 1.2.

$$n_i(x + \Delta x, t + \Delta t) = n_i(x, t) + \Lambda_i(n(x, t)) \quad (1.1)$$

$$\Lambda_i = n_{i\oplus 1}n_{i\oplus 3}(1 - n_i)(1 - n_{i\oplus 2}) - (1 - n_{i\oplus 1})(1 - n_{i\oplus 3})n_in_{i\oplus 2} \quad (1.2)$$

In Eq. 1.2 \oplus is the modulus operator. The collision operator, Λ , conserves mass, momentum, and energy, which is readily shown by taking the first 3 moments of Λ about the velocity, c_i , as given in Eq. 1.3.

$$\begin{aligned} \sum_{i=1}^4 \Lambda_i &= 0 \\ \sum_{i=1}^4 c_i \Lambda_i &= 0 \\ \sum_{i=1}^4 c_i^2 \Lambda_i &= 0 \end{aligned} \quad (1.3)$$

Macroscopic variables are obtained by taking moments of the probability distribution function, f , about the velocity, c_i , as shown in Eq. 1.4. The probability distribution function describes the distribution of atoms throughout the lattice. For fluid and thermal applications the distribution function is accurately described by a Maxwellian distribution.¹³

$$\begin{aligned} \rho &= \sum_{i=1}^4 m f_i \\ \rho u &= \sum_{i=1}^4 m c_i f_i \end{aligned} \quad (1.4)$$

In Eq. 1.4 m is mass, ρ is density, and ρu is momentum. The particle's probability distribution function, f , is difficult to derive, thus it is often replaced by a spatial and/or temporal average at the node of interest.¹⁴

Streaming

The main benefit of LGA and LBM is the separation of the streaming and collision operations. This allows parallel deployment on GPU architectures,¹⁵ dramatically reducing simulation time. The streaming step propagates the information in a specific direction. This

is shown mathematically in Eq. 1.5.

$$n_i(x + \Delta x, t + \Delta t) = n_i(x, t) \tag{1.5}$$

Intuitively one can see that a particle will stream in the same direction without change if there are no other particles to collide with, which is also a paraphrase of Newton's first law. There needs to be a mechanism that can alter the trajectory of the particle. In LGA and LBM this mechanism is the collision operator.

Colliding

The collision operator, Λ_i as shown in Eq. 1.6, is the only mechanism that prevents a particle from following a specific trajectory indefinitely.

$$n_i(x + \Delta x, t + \Delta t) = n_i(x, t) + \Lambda_i(x, t) \tag{1.6}$$

The collision operator is discussed later in this chapter, so it will suffice to mention here that the collision operator is the heart of LBM models. Local physics are conserved during the collision step.

1.2.2 LBM Lattice Configurations

LGA and LBM are employed on nodes in discretized space. A common nomenclature for lattice configurations is $D_n Q_m$ where n is the dimension of the problem (1, 2, or 3) and m is the number of directions used to discretize the domain space. Lattice configurations for one dimensional, two dimensional, and three dimensional domains are shown in Fig. 1.1 and Fig. 1.2.

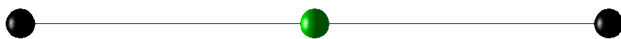


Figure 1.1: *One dimensional LBM lattice configuration.*

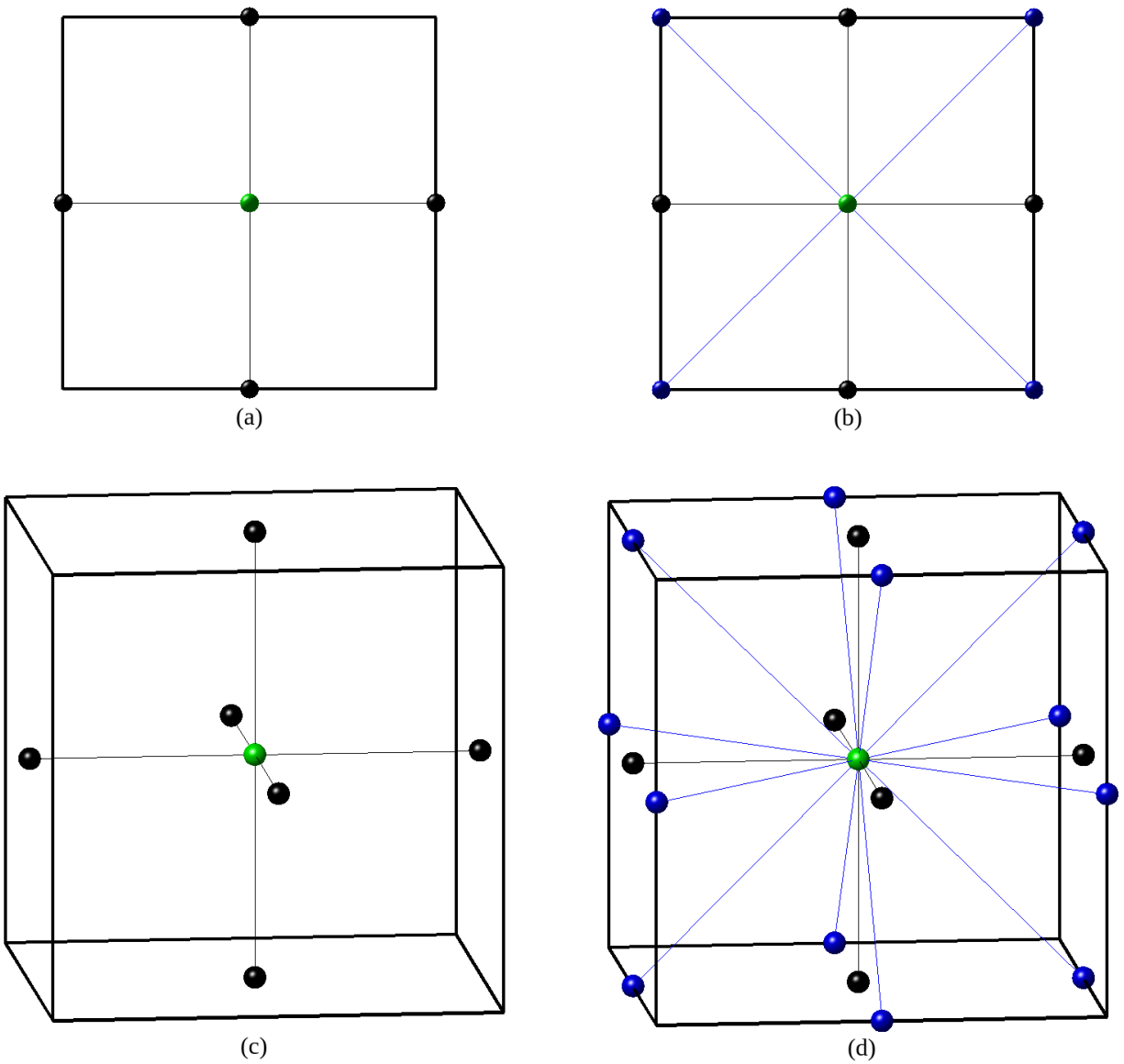


Figure 1.2: *Various two and three dimensional LBM lattice configurations showing (a) D_2Q_5 , (b) D_2Q_9 , (c) D_3Q_7 , and (d) D_3Q_{19} lattices.*

1.2.3 Benefits and Drawbacks of LGA

The main advantages of LGA are that it has no truncation error because the collision operator is boolean, it is relatively easy to understand and implement, and it is very parallelizable due to the fact that the collision operator relies only on local variables.

There are, however, certain drawbacks that keep the model from being sufficient for representing hydrodynamic flow. Among these drawbacks are statistical noise from the boolean variables, violation of Galilean invariance, and a dependence of velocity on pressure.¹⁴ LGA lacks rotational invariance due to only describing motion in the 4 cardinal directions, thus vortices appear as squares. Galilean invariance was restored by adding more directional components to the model, for example using a D_2Q_9 lattice instead of a D_2Q_5 lattice.

1.2.4 LBM from LGA

LBM operates with the same stream and collision mechanics as LGA, however various improvements freed LBM from the shortcomings associated with LGA mentioned in the previous section. The most significant improvement was the simplification of the collision operator that reduced the boolean noise. Various methods have been employed to reduce the complexity of the collision operator in LGA. Bhatnagar, Gross, and Krook developed a simplified model (BGK approximation) based on the assumption that the collision operator returns nothing at equilibrium, thus $\Lambda(f^{eq}, f^{eq}) = 0$ ¹⁶. They represented their model as

$$\Lambda_i(f) = -\frac{1}{\tau}(f_i - f_i^{eq}) \quad (1.7)$$

where Λ is the collision operator, f is a probability distribution function (pdf), τ is a relaxation parameter, and i is a discrete direction. McNamara and Zanetti first introduced a distribution function in order to reduce statistical noise and simplify the collision operator.¹⁷ Higuera and Jimenez further simplified the collision operator by linearizing the model based on the assumption that the distribution, f , was close to equilibrium.¹⁸ The collision operator

was simplified even more by several groups working independently from each other,^{19,20,21} with the resulting model having a similar structure to the BGK model as given by Eq. 1.7. The main difference in these models is their handling of the relaxation parameter, τ .

In 1872 Ludwig Boltzmann showed that any system of ideal gas, regardless of its initial distribution, will reach equilibrium as a Maxwellian distribution.^{22,13} By using a Maxwellian distribution function in the collision operator statistical noise is significantly reduced, due to the calculated probabilities being rational numbers.

For fluid mechanics the equilibrium distribution approaches a Maxwellian distribution, however for radiative transport this does not hold true. Fluid simulations necessarily take into account inter-particle collisions, thus the number of collisions is proportional to the gradient of the concentration of particles at a given location. The inter-particle collision rate of radiation particles is negligible. For this reason the collision operator for radiative transport is linear and can be described by absorption and scattering integrals. A scattering collision operator for the RTE is thus given by

$$\Lambda_s = \omega w \sum_{i=1}^Q I(\vec{r}, \vec{\Omega}, E, t) \quad (1.8)$$

where ω is the scattering albedo, w is directional weight, Q is the number of discrete LBM directions and $I(\vec{r}, \vec{\Omega}, E, t)$ is the intensity of radiation at position \vec{r} traveling in a direction $\vec{\Omega}$ with energy E at time t .

1.3 Boundary Conditions for LBM

The streaming operation carries information from the boundary to the rest of the domain, as shown in Eq. 1.9,

$$n_i(x + \Delta x, t + \Delta t) = n_i(x, t) + \Lambda_i(x, t) \quad (1.9)$$

however the boundary receives no value from either the streaming operation or the collision operation. The boundary conditions thus need to be specified depending on the local physics at each boundary.

Common boundary conditions for fluid mechanics are periodic, no-slip (also known as bounceback), and sliding wall. The periodic boundary conditions are generally used to simulate a repeating representative cell of a much larger domain. No-slip conditions are typically referred to as bounceback boundary conditions, due to how they are enforced in LBM. When the fluid reaches a wall during the streaming step then the next streaming step mirrors the distributions at the surface, effectively "bouncing" what came in off of the wall. The sliding wall condition is used to allow movement of the bounding surface. These boundary conditions are enforced by using only the components of the discrete velocities moving parallel to the surface.

The physics for radiative transport are much different than for fluid mechanics, thus new boundary conditions need to be introduced for the case of the RTE. The physics occurring at the interface include transmission, reflection and emission of radiation.

Boundary conditions for LBM which can be applied to the RTEs include periodic and fixed conditions for radiative flux and partial currents. Periodic conditions are used the same way as described for fluid mechanics, what goes out one side comes in the opposite side. Dirichlet conditions can be used to specify a known flux at the surface. The equivalent direction dependent flux distributions at the boundaries can be used to specify the partial currents and gradient of the flux, or the net current at the surface.

Transmission of radiation is defined as radiation passing through a material. Radiative emission particularly relevant for radiative heat transfer problems is the radiative flux emitted by the surface based on the temperature and emissivity of the object. Together these correspond to a known radiative flux at the boundary, which can be modeled as a Dirichlet boundary condition, for which the boundary value is specified. For example, consider solar radiation incident upon a car windshield. Some radiation passes through, while some is

reflected from the windshield surface. At the same time the windshield, which has a temperature of its own, is emitting thermal radiation. The total amount of thermal radiation entering the car is the sum of the transmitted and emitted radiations.

To enforce a Dirichlet boundary condition the radiative intensity on a boundary node is specified, as shown in Eq. 1.10,

$$I_i(\vec{r}, t) = I_o, \quad \vec{r} \in \text{boundary} \quad (1.10)$$

where I_o is the specified radiative intensity. In this work Dirichlet boundary conditions are employed mainly for thermal radiation simulations where the emission is based on a known material temperature and a known material emissivity. Details are provided in Ch. 2.

1.4 Directions and Weight Factors

The most common form of LBM is implemented on a Cartesian grid. This means that the distance radiation travels in each direction is unique. The time step for propagating radiation in each direction is the same, and the velocity of the radiation is the same in all directions, thus a weight factor must be introduced to artificially synchronize the transport of radiation for a single time step. In this regard LBM is similar to DOM. While DOM weight factors are derived from geometrical relations, LBM weight factors are derived from generalized lattice tensors²³. The difference between propagation in a single step of LBM versus DOM is shown in Fig. 1.3.

With LBM the radiation traveling in each direction extends completely to the next grid location where the solution is sought. In order to account for the varying distances traveled by each direction apparent discrete velocities are calculated using Eq. 1.11.

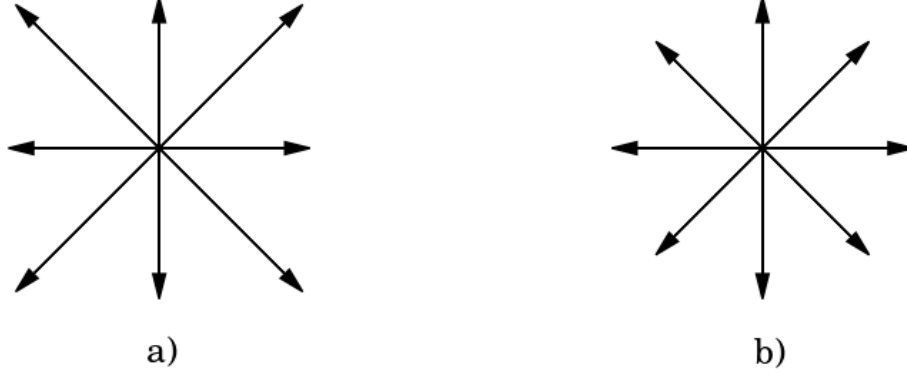


Figure 1.3: Distances traveled in each direction in a single time step using a) LBM and b) DOM methods.

$$c_i = \begin{cases} c \left(\cos \left(\frac{(i-1)\pi}{2} \right), \sin \left(\frac{(i-1)\pi}{2} \right) \right) & i = 1, 2, 3, 4 \\ \sqrt{2}c \left(\cos \left(\frac{(i-5)\pi}{2} + \frac{\pi}{4} \right), \sin \left(\frac{(i-5)\pi}{2} + \frac{\pi}{4} \right) \right) & i = 5, 6, 7, 8 \end{cases} \quad (1.11)$$

The discrete velocities are used to determine appropriate weight factors, w_i , through tensor moment expansions²³. Along with maintaining consistent radiation propagation in each direction, weight factors are needed to preserve rotational invariance.²⁴ Rotational invariance means that the lattice can be rotated in 90° increments without changing the results. This is a necessary feature in LBM because the streaming operation is the same in each direction. Jeffreys explains that a rotationally invariant Cartesian lattice must satisfy the conservation equations, which are moments about the lattice speed²⁵. Odd moments will vanish due to symmetry and even moments can be used to find the weight factors and directional lattice speeds.

For the D_2Q_8 lattice (radiation has no stationary node) which has discrete velocities

shown in Eq. 1.11 the odd moment equations vanish due to symmetry

$$\begin{aligned}\sum_{i=1}^8 c_{i\alpha} w_i &= 0 \\ \sum_{i=1}^8 c_{i\alpha} c_{i\beta} c_{i\gamma} w_i &= 0\end{aligned}\tag{1.12}$$

and the even moments can be expressed as

$$\begin{aligned}\sum_{i=1}^8 w_i &= 1 \\ \sum_{i=1}^8 c_{i\alpha} c_{i\beta} w_i &= \delta_{\alpha\beta} \\ \sum_{i=1}^8 c_{i\alpha} c_{i\beta} c_{i\gamma} c_{i\eta} w_i &= \delta_{\alpha\beta} \delta_{\gamma\eta} + \delta_{\alpha\gamma} \delta_{\beta\eta} + \delta_{\alpha\eta} \delta_{\beta\gamma}\end{aligned}\tag{1.13}$$

where δ is the Kronecker Delta function. Jeffreys showed that any higher order tensor can be represented as a combination of 2nd and 4th order tensors. Similarly 4th order tensors can be represented as a combination of 2nd order tensors. Noting that the velocities evaluate to

$$c_i = c \cdot \begin{cases} (1, 0), (0, 1), (-1, 0), (0, -1) & i = 1, 2, 3, 4 \\ (1, 1), (-1, 1), (-1, -1), (1, -1) & i = 5, 6, 7, 8 \end{cases}\tag{1.14}$$

Table 1.1: Directional weights for one dimensional and two dimensional lattices used in radiative simulations.

Lattice	Direction, i	Weight, w_i
D ₁ Q ₂	1-2	0.50
D ₂ Q ₄	1-4	0.25
D ₂ Q ₈	1-4	0.20
	5-8	0.05

Eq. 1.13 can be expanded to

$$\begin{aligned}
 \sum_{i=1}^Q w_i &= 4w_1 + 4w_2 = 1 \\
 \sum_{i=1}^Q c_{i1}^2 w_i &= 2c^2 w_1 + 4c^2 w_2 = 1 \\
 \sum_{i=1}^Q c_{i1}^4 w_i &= 2c^4 w_1 + 4c^4 w_2 = 3 \\
 \sum_{i=1}^Q c_{i1}^2 c_{i2}^2 w_i &= 4c^4 w_2 = 1
 \end{aligned} \tag{1.15}$$

Eq. 1.15 is a system of four equations with three unknowns. A unique solution is obtained by requiring the weights to be non-negative and non-zero. With these constraints, and by keeping c arbitrary, solving these moment equations for the two unique directional weights yields $w_1 = \frac{1}{5}$ and $w_2 = \frac{1}{20}$, where 1 and 2 correspond to cardinal and diagonal directions, respectively. Another point of interest is that in fluid mechanics a rest velocity is assigned to node 0, the central node. For radiative transfer a stationary node is not physically possible, thus stationary weights are always 0 for radiation LBM lattices. Tab. 1.1 gives the weights for various one dimensional and two dimensional lattices with varying numbers of discrete directions.

1.5 Radiative Transport LBE

For radiation moving through a material the general form of the RTE can be written as²⁶

$$\begin{aligned} \frac{1}{c} \frac{\partial I(\vec{r}, \vec{\Omega}, t, E)}{\partial t} + \vec{\Omega} \cdot \nabla I(\vec{r}, \vec{\Omega}, t, E) = \\ \kappa_a I_b(\vec{r}, \vec{\Omega}, t, E) - \kappa_a I(\vec{r}, \vec{\Omega}, t, E) - \sigma_s(\vec{r}, \vec{\Omega}, t, E) I(\vec{r}, \vec{\Omega}, t, E) + \\ \frac{\sigma_s}{4\pi} \int_{4\pi} I(\vec{r}, \vec{\Omega}', t, E') \Phi(\vec{\Omega}' \rightarrow \vec{\Omega}, E' \rightarrow E) d\vec{\Omega}' \quad (1.16) \end{aligned}$$

where c is velocity, $I_b(\vec{r}, \vec{\Omega}, t, E)$ is the blackbody radiative intensity, $I(\vec{r}, \vec{\Omega}, t, E)$ is the radiative intensity at position \vec{r} with direction $\vec{\Omega}$ at time t with energy E , κ_a is the absorption coefficient, σ_s is the scattering coefficient, and $\Phi(\vec{\Omega}' \rightarrow \vec{\Omega}, E' \rightarrow E)$ is the scattering phase function which describes the probability of scattering into direction $\vec{\Omega}$ from an initial direction $\vec{\Omega}'$. The first and second terms on the left hand side of Eq. 1.16 represent the temporal and spatial change in radiative intensity, respectfully. The first term on the right is the source of radiation due to black body radiation. The second and third terms account for radiation sinks due to absorption and scattering with the medium. The fourth term is a source due to in-scattered radiation, or radiation that initially had a different direction and energy, but after scattering has the same energy and direction as that being considered. For isotropic scattering the probability of scattering from any direction into any other direction is equal, thus the scattering phase function is simply unity, $\Phi(\vec{\Omega}_i, \vec{\Omega}) = 1$.

Normally the scattering integral calculation is resource consuming due to the necessity of evaluating radiative contributions from every other node. Thus the evaluation of intensity at a point relies on a multidimensional integral. Due to the nature of LBM, directional information at each individual node can be used to determine the macroscopic quantities. What would in other methods be a recursive integral becomes a local summation. This is the main benefit of using the LBM for radiative transport. The ability of LBM to conserve macroscopic quantities is paramount in the implementation.

Bindra¹ showed that the corresponding LBE for the monoenergetic RTE conserves macroscopic energy and can be written as

$$\begin{aligned} \nabla I(\vec{r} + c_{\vec{\Omega}}\Delta t, \vec{\Omega}, t + \Delta t) - \nabla I(\vec{r}, \vec{\Omega}, t) = \\ \frac{\Delta x}{\vec{\Omega}} \left[\kappa_a I_b(\vec{r}, \vec{\Omega}, t) - \kappa_a I(\vec{r}, \vec{\Omega}, t) - \sigma_s(\vec{r}, \vec{\Omega}, t) I(\vec{r}, \vec{\Omega}, t) + \right. \\ \left. \frac{\sigma_s}{4\pi} \sum_{i=1}^Q I(\vec{r}, \vec{\Omega}_i, t) \Phi(\vec{\Omega}_i, \vec{\Omega}) \right] \end{aligned} \quad (1.17)$$

where $S(\vec{r}, \vec{\Omega}, t)$ is a source term representing radiative emission from within the media and $w_{\vec{\Omega}}$ is a weight factor for direction $\vec{\Omega}$. The source term is analogous to an external force term in the LBE for fluid mechanics as derived by He and Guo.^{27,28} It can be seen that the volumetric integral has been replaced by a nodal summation across all discrete directions, Q . Numerical accuracy is important when representing the macroscopic quantities because of error propagation. A Taylor series expansion can be used to determine the expected numerical accuracy of the aforementioned LBE as a function of grid size.

The Taylor series expansion of Eq. 1.17 in space and time, and noting that $\Delta\vec{r} = c\Delta t$, leads to

$$I(\vec{r} + c\Delta t, \vec{\Omega}, t + \Delta t) \approx I(\vec{r}, \vec{\Omega}, t) + \frac{\partial I(\vec{r}, \vec{\Omega}, t)}{\partial t} \Delta t + \frac{\partial I(\vec{r}, \vec{\Omega}, t)}{\partial \vec{r}} c\Delta t + O(\Delta t^2) \quad (1.18)$$

Inserting Eq. 1.18 into Eq. 1.17 and dividing by Δt yields

$$\begin{aligned} \frac{1}{c} \frac{\partial I(\vec{r}, \vec{\Omega}, t)}{\partial t} + \frac{\partial I(\vec{r}, \vec{\Omega}, t)}{\partial \vec{r}} = \\ - \kappa_a I(\vec{r}, \vec{\Omega}, t) + w(\vec{\Omega}) \sum_i \Phi(\vec{\Omega}, \vec{\Omega}_i) I(\vec{r}, \vec{\Omega}_i, t) + S(\vec{r}, \vec{\Omega}, t) + O(\Delta t) \end{aligned} \quad (1.19)$$

It is worth mentioning that while the LBM for the RTE is first order accurate, the LBM for fluid mechanics is claimed to be second order accurate in computing velocity.²⁴

More details on the LBE formulation will be provided in the next chapters along with some example problems.

Chapter 2

One Dimensional Multiple-Mode

Heat Transfer

2.1 Introduction

Over the last two decades the number of high temperature applications has dramatically increased due to the advances made in material science. Some of these industrial applications include the manufacturing of glass, design of insulating material, porous burners, solar collectors, high temperature nuclear reactors, etc. Designing high temperature applications requires a knowledge of the volumetric radiation because at higher temperatures radiative contributions from each component increases.

In many engineering calculations thermal radiation is quantified by a surface-to-surface radiative exchange via the Stefan-Boltzmann equation.⁹ View factors are used to relate the fractional amount of radiation that leaves a body and interacts with another body. These types of models assume no interaction of radiation with the medium of propagation separating two surfaces. This simple model cannot be applied if the medium between the bodies has a relatively high degree of interaction with the radiation being emitted from the surfaces.

There are various numerical methods and codes available which can solve for radiative heat transfer within a participating media, as mentioned in the last chapter, but practical problems of high temperature applications involve continuum mechanics of the participating media and also account for other modes of energy exchange. In a multi-physics simulation evaluating the radiative heat transfer in conjunction with other heat transfer modes requires tightly coupled simulations. Therefore a simplified deterministic method is required for multi-physics applications which can reduce the computational demands of the RTE while still being able to solve continuum mechanics as well. This chapter shows how LBM compares to existing methods, namely the Spherical Harmonics P_1 method, for multi-mode one dimensional problems.

2.2 Mathematical Formulation

This chapter considers radiation-material interactions for homogeneous materials with isotropic scattering. For these conditions the governing equations for non-equilibrium monoenergetic radiative transfer and energy transport are given by

$$\frac{1}{\nu} \frac{\partial I(\vec{r}, \vec{\Omega}, t)}{\partial t} + \vec{\Omega} \nabla I(\vec{r}, \vec{\Omega}, t) = \kappa_a \left[\frac{1}{4\pi} \sigma T(\vec{r}, t)^4 - I(\vec{r}, \vec{\Omega}, t) \right] + \sigma_s \left[\frac{1}{4\pi} \int_{4\pi} I(\vec{r}, \vec{\Omega}, t) d\vec{\Omega} - I(\vec{r}, \vec{\Omega}, t) \right] + S(\vec{r}, \vec{\Omega}, t) \quad (2.1)$$

and

$$\rho C_p \frac{\partial T(\vec{r}, t)}{\partial t} = \nabla \cdot (k \nabla T) + \kappa_a \left[\int_{4\pi} I(\vec{r}, \vec{\Omega}, t) d\vec{\Omega} - \sigma T(\vec{r}, t)^4 \right]. \quad (2.2)$$

In Eq. 2.1 $I(\vec{r}, \vec{\Omega}, t)$ is the radiative intensity at a spatial location \vec{r} with direction $\vec{\Omega}$ at time t , ν is the speed of the radiation, κ_a is the absorption coefficient, σ_s is the scattering coefficient and $S(\vec{r}, \vec{\Omega}, t)$ is the volumetric energy source at \vec{r} with direction $\vec{\Omega}$ at time t . The terms on the left side of the Eq. 2.1 account for changes in the radiative field due to

temporal and spatial effects. For steady-state problems the temporal term goes away. The first two terms on the right of Eq. 2.1 represent radiative source and sink terms due to absorption. Likewise the third and fourth terms represent source and sink terms due to scattering events. The last term on the right side of Eq. 2.1 represents all external source terms other than those from absorption and scattering of radiation. In the energy transport equation, Eq. 2.2, $T(\vec{r}, t)$ is the temperature at \vec{r} and time t , ρ is density, C_p is specific heat, σ is the Stefan-Boltzmann constant, V is volume and k is thermal conductivity. The first term on the left of Eq. 2.2 represents the temporal change in temperature. For steady-state problems this term goes away. The first term on the right represents thermal diffusion via conduction. This term goes away for media with infinite thermal resistance, such as air. The second and third terms represent source and sink terms due to radiation absorption and emission, respectively.

2.3 Numerical Examples

2.3.1 Radiation: Su-Olson Wave

Su and Olson published an analytical solution to the problem of non-equilibrium radiative transport in a one dimensional participating media.²⁹ The problem considered has a source term appearing in the radiation equation, which changes the temperature profile along the one dimensional slab. The heated slab emits radiation, which appears as a source term in the RTE. Note that the coupled differential equations are linearized before being solved by assuming that κ_a and σ_s are constant and that C_p is proportional to the cube of the temperature, $C_p \propto T^3$.³⁰ This coupled behavior is captured for the transient case. For this problem thermal resistance is neglected and the one dimensional radiation and energy

equations become

$$\begin{aligned} \frac{1}{\nu} \frac{\partial I(x, \mu, t)}{\partial t} + \mu \frac{\partial I(x, \mu, t)}{\partial x} = \kappa_a \left[\frac{1}{2} \sigma T(x, t)^4 - I(x, \mu, t) \right] \\ + \sigma_s \left[\frac{1}{2} \int_{-1}^1 I(x, \mu, t) d\mu - I(x, \mu, t) \right] + S(x, \mu, t) \end{aligned} \quad (2.3)$$

and

$$\rho C_p \frac{\partial T(x, t)}{\partial t} = \kappa_a \left[\int_{-1}^1 I(x, \mu, t) d\mu - \sigma T^4(x, t) \right] \quad (2.4)$$

where μ is the direction cosine that describes the direction of motion of the radiation.

The radiative field is found by solving Eq. 2.3 with LBM using the approach described in Ch. 1. In this problem the source term $S(x, \mu, t)$ appearing in Eq. 2.3 is a finite source in time and space. The source is turned on for a specified time between $-x_o$ and x_o , as shown in Eq. 2.5

$$\begin{aligned} S(x, \mu, t) &= \frac{1}{2} S_x(x, \mu) S_t(t, \mu) \\ S_x(x, \mu) &= \frac{1}{2x_o} [H(x + x_o) - H(x - x_o)] \\ S_t(t, \mu) &= H(t) - H(t - t_o) \end{aligned} \quad (2.5)$$

where x_o and t_o are initial conditions.

Through the simplifying assumptions mentioned, the equations for radiation and energy can be linearized. By defining non-dimensional variables $\Psi(x, \mu, t) = \frac{I(x, \mu, t)}{\sigma T_r^4}$, $\theta(x, t) = \frac{T(x, t)^4}{T_r^4}$ and $s(x, \mu, t) = \frac{S(x, \mu, t)}{\sigma T_r^4}$ the coupled linear differential equations for radiation and energy become

$$\begin{aligned} \frac{1}{\nu} \frac{\partial \Psi(x, \mu, t)}{\partial t} + \mu \frac{\partial \Psi(x, \mu, t)}{\partial x} = \\ \kappa_a \left(\frac{1}{2} \theta(x, t) - \Psi(x, \mu, t) \right) + \sigma_s \left(\frac{1}{2} \int_{-1}^1 \Psi(x, \mu, t) d\mu - \Psi(x, \mu, t) \right) + s(x, \mu, t) \end{aligned} \quad (2.6)$$

and

$$\rho \frac{\partial \theta(x, t)}{\partial t} = \kappa_a \left[\int_{-1}^1 \Psi(x, \mu, t) d\mu - \theta(x, t) \right] \quad (2.7)$$

For this example $\kappa_a = 1$, $\sigma_s = 0$, $\nu = 1$, $x_o = 0.5$, $\rho = 1$ and $t_o = 10$. The cardinal directions for this problem are $\mu = \pm \frac{1}{\sqrt{3}}$ and the initial profile and boundary conditions are given by Eq. 2.8. It is important to note that the values of μ come from truncating the expansion representing angular discretization, similar to P_1 methods where, in many instances, polynomials higher than $P_2 = \frac{1}{2}(3\mu^2 - 1)$ are assumed to have a negligible contribution and are thus ignored.

$$\begin{aligned} \Psi_\mu(x = -\infty, t) &= 0 \\ \Psi_{-\mu}(x = \infty, t) &= 0 \\ \Psi_{\pm\mu}(x, t = 0) &= 0 \end{aligned} \quad (2.8)$$

A half domain of $L = 10x_o$ was used in the simulation. The results in Fig. 2.1 show excellent agreement between LBM and the analytical solution.

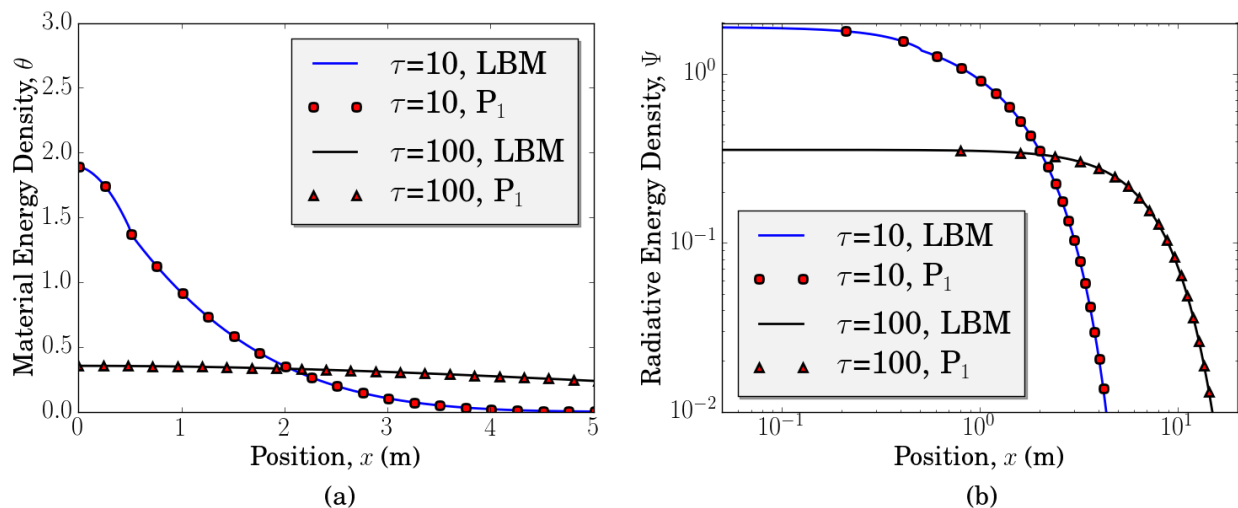


Figure 2.1: *Su-Olson* results for the case of $\kappa_a = 1$, $\sigma_s = 0$, $\nu = 1$, $x_o = 0.5$, $\rho = 1$ and $t_o = 10$.

2.3.2 Radiation-Conduction: One Dimensional Media

Formulation

The previous example demonstrated the capability of LBM to solve a set of linear non-equilibrium RTE and energy transport equations without spatial resistance. In a more realistic example for a stationary participating media, the emissive term is non-linear and the heat conduction term is finite. This work solves the non-linear coupled interaction using LBM for both the radiation and the energy equations with the heat conduction term.

For this example LBM is used to find the steady-state radiation and energy profiles of a slab of participating material with fixed outer temperatures. The one dimensional steady-state representations of Eq. 2.1 and Eq. 2.2 describing radiation and material temperature are given in Eq. 2.9 and Eq. 2.10, respectively.²³

$$\mu \frac{dI(x, \mu)}{dx} = \kappa_a \left[\frac{1}{2} \sigma T(x)^4 - I(x, \mu) \right] + \sigma_s \left[\frac{1}{2} \int_{-1}^1 I(x, \mu) d\mu - I(x, \mu) \right] + S(x, \mu) \quad (2.9)$$

$$k \frac{d^2 T}{dx^2} = \kappa_a \left(\sigma T^4 - \int_{-1}^1 I(x, \mu) d\mu \right) \quad (2.10)$$

In Eq. 2.10 k is thermal conductivity, T is material temperature, σ is the Boltzmann constant, κ_a is the absorption coefficient, I is the intensity of radiation and μ is the direction cosine. The non-dimensional forms of Eq. 2.9 and Eq. 2.10 can be obtained by making the following substitutions:

$$\begin{aligned} \tau_x &= \frac{\beta x}{\tau_L} & \tau_L &= \beta L & N &= \frac{k\beta}{4\sigma T_L^3} \\ \theta &= \frac{T}{T_L} & \Psi &= \frac{I}{\sigma T_L^4} & S^* &= \frac{S}{\sigma T_L^4} \end{aligned} \quad (2.11)$$

The resulting dimensionless equations are shown in Eq. 2.12 and Eq. 2.13 for radiation and

energy, respectively.

$$\mu \frac{d\Psi(\tau_x, \mu)}{d\tau_x} = (1 - \omega) \frac{\theta^4(\tau_x)}{2} - Psi(\tau_x, \mu) + \frac{\omega}{2} \int_{-1}^1 \Psi(\tau_x, \mu) d\mu \quad (2.12)$$

$$\frac{\partial^2 \theta(\tau_x)}{\partial \tau_x^2} = \frac{1 - \omega}{N} \left(\theta^4(\tau_x) - \int_{-1}^1 \Psi(\tau_x, \mu) d\mu \right) \quad (2.13)$$

where τ_x is the non-dimensional optical thickness in the x direction, N is the conduction-radiation parameter, otherwise known as the Stark number, that relates radiative and conductive heat fluxes, $\omega = \frac{\sigma_s}{\kappa_a + \sigma_s}$ is the scattering albedo, θ is the dimensionless temperature and I is the dimensionless radiation intensity. It should be mentioned that, by definition, $\kappa_a = \beta - \sigma_s$. Thus, $\frac{\kappa_a}{\beta} = \frac{\beta}{\beta} - \frac{\sigma_s}{\beta} = 1 - \omega$. The LBE's for Eq. 2.12 and Eq. 2.13 are given by Eq. 2.14 and Eq. 2.15 as shown in Ch. 1 and literature,^{13,23} respectively.

$$\begin{aligned} \Psi_i(\tau_x + \Delta\tau_x, t + \Delta t) = & \Psi(\tau_x, t) + \\ & \Delta t \left[-\Psi(\tau_x, t) + (1 - \omega)w_i\theta^4(\tau_x, t) + \omega w_i \sum_j \Psi_j(\tau_x, t) \right] \end{aligned} \quad (2.14)$$

$$\begin{aligned} f_i(\tau_x + \Delta\tau_x, t + \Delta t) = & f_i(\tau_x, t) - \frac{1}{c_s^{-2} + 0.5\Delta t} [f_i(\tau_x, t) - f_i^{eq}(\tau_x, t)] + \\ & w_i \left(\frac{1 - \omega}{N} \left(\theta^4(\tau_x, t) - \frac{1}{4} \sum_j \Psi_j(\tau_x, t) \right) \right) \Delta t \end{aligned} \quad (2.15)$$

In Eq. 2.14 the scattering integral is approximated by numerical quadrature and w_i are the weights associated with the i^{th} direction. In Eq. 2.15 $c_s = \frac{\Delta x}{\Delta t}$ is the lattice speed, f_i is the distribution function and f_i^{eq} is the equilibrium distribution function. The non-dimensional temperature variable, θ , couples the radiation and material energy equations.

Boundary conditions for the radiation equation are calculated based on emissivities of

the walls along with the known temperatures at the boundary, as shown in Eq. 2.16.

$$\Psi_w = \varepsilon\theta_w^4 + \frac{(1 - \varepsilon)}{4\pi} \int_{|\vec{n} \cdot \mu' < 0|} \Psi(\mu' \rightarrow \mu) d\mu' \quad (2.16)$$

In Eq. 2.16 Ψ_w is the non-dimensional radiative intensity at the wall, ε is the emissivity of the wall, θ_w is the temperature at the wall and \vec{n} is the outward normal of the wall.

Modest gives the dimensionless equations for the P_1 approximation for this one dimensional slab geometry as³¹

$$\frac{d^2 G}{d\tau_x^2} + 3(\theta^4 - G) = 0 \quad (2.17)$$

$$\frac{d^2 \theta}{d\tau_x^2} = \frac{1}{N}(\theta^4 - G) \quad (2.18)$$

$$\frac{dG}{d\tau_x} + \frac{3}{2} \frac{\varepsilon_L}{2 - \varepsilon_L} (1 - G) = 0 \quad \tau = 0 \quad (2.19)$$

$$\frac{dG}{d\tau_x} - \frac{3}{2} \frac{\varepsilon_R}{2 - \varepsilon_R} (\theta_R^4 - G) = 0 \quad \tau_x = \tau_L \quad (2.20)$$

In Eq. 2.17 through Eq. 2.20 G is the non-dimensional total radiative flux, τ_x is the optical thickness and ε_L and ε_R are the emissivities of the left and right faces, respectively.

Results

The steady-state results with a two directional LBM in one dimension (D_1Q_2) using $w_{1,2} = 0.5$ are compared with P_1 benchmark solutions. The effect of Stark number, N , is shown in Fig. 2.2 for (a) walls with emissivities of $\varepsilon_1 = \varepsilon_2 = 0$ and (b) walls with emissivities $\varepsilon_1 = \varepsilon_2 = 1$. The time step for each simulation is $\Delta t = \Delta \tau = \frac{1}{N_x - 1}$ where $N_x = 1000$ is the number of nodes used to discretize the domain. Direction cosines are $\mu = \pm \frac{1}{\sqrt{3}}$. The media is non-scattering, $\omega = 0$. Effect of emissivities are shown in Fig. 2.3.

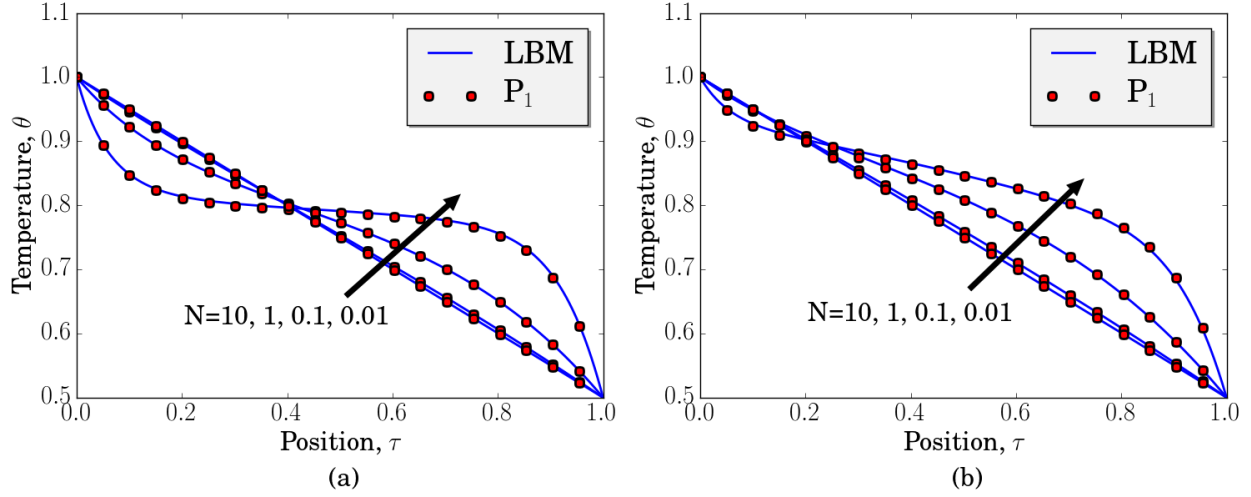


Figure 2.2: Temperature profile with varying optical thicknesses. $\theta_L = 1$, $\theta_R = 0.5$, $\tau_L = \kappa_a L = 1$ and (a) $\varepsilon_0 = \varepsilon_2 = 0$ (b) $\varepsilon_1 = \varepsilon_2 = 1$.

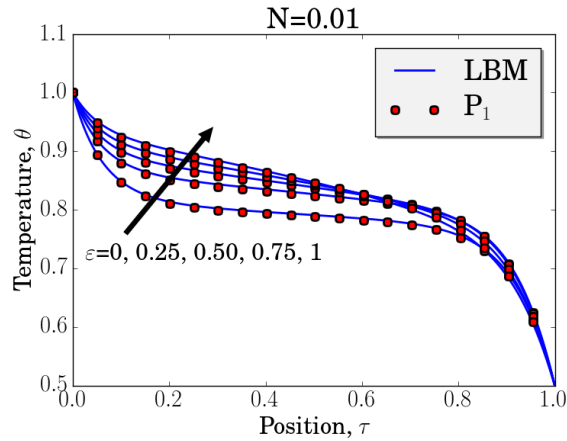


Figure 2.3: Temperature profile with varying optical thicknesses. $N = 0.01$, $\theta_L = 1$, $\theta_R = 0.5$ and $\tau_L = \kappa_a L = 1$.

Error Analysis

It was shown in Ch. 1 that LBM for radiative transfer is first order accurate. The grid convergence results presented in Fig. 2.4 show that error, as defined by Eq. 2.21, reduces linearly with grid size. Other established methods such as DOM can also be first order

accurate, depending on the level of truncation.³²

$$Error = \frac{\theta_{new} - \theta_{old}}{\theta_{old}} \quad (2.21)$$

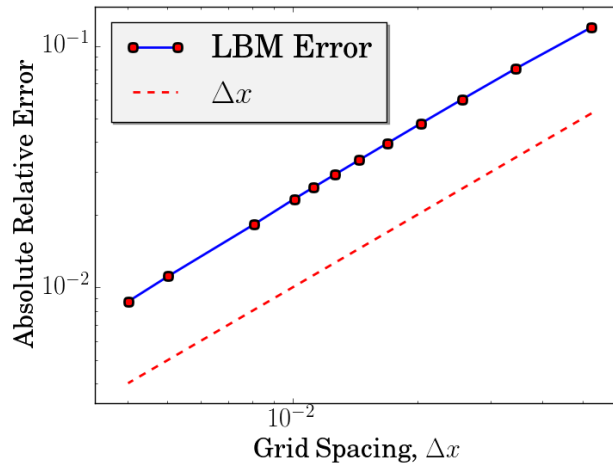


Figure 2.4: Error as a function of node spacing for the participating slab example. The slope of the log of the error follows a 1:1 ratio with Δx , thus the method is observed to be first order accurate.

It can be seen in Fig. 2.4 that the slope of the error follows a first order slope, thus the observed order of accuracy is first order.

2.4 Conclusions

The LBM based RTE models were extended for their application into coupled multi-physics problems. The results of this chapter on simple examples in multi-mode heat transfer show that LBM has potential in solving coupled multi-physics problems. A benchmark problem with conduction-radiation heat transfer in a slab geometry was solved using a LBM model and results are in good agreement with the benchmark P_1 results. Agreement between P_1 and LBM is expected because in the limit of $\Delta x \rightarrow 0$ the methods become identical. The effect of Stark number and wall emissivity on thermal behavior was studied. A grid

convergence study was performed which showed that LBE for RTE's is a first order accurate method.

This chapter introduced the application of LBM to coupled radiation-conduction problems in one dimension. The non-linear emissivity source term with uniform weight distribution was modeled in LBM. The results showed that LBM is comparable to the P_1 method for one dimensional problems.

Chapter 3

Two Dimensional Multiple-Mode Heat Transfer

3.1 Introduction

Most multi-mode heat transfer problems can be modeled practically in two or three dimensions. This chapter extends the multi-mode work into two dimensions. Models for fluid flow and convective heat transfer are coupled to the previous models of conduction and radiation. A LBM framework to solve multiphysics problems is developed and implemented to solve the case of a porous burner with convection, conduction, radiation and fluid flow. Mathematical formulations are explained in detail in Ch. 2.

3.2 Radiative Validation

LBE solutions to two dimensional RTE problems were developed by Bindra¹ and Asinari¹⁰. In one basic two dimensional example the temperature of the entire domain is kept constant and the radiative flux was computed using a D_2Q_4 lattice. Prior to adopting higher accuracy lattices for multi-mode heat transfer problems, such as the D_2Q_8 lattice introduced in Ch. 1,

these higher angular resolution schemes must be validated for the single physics of radiative transport. To validate the radiative component of the simulations in this chapter LBM was compared to DOM for the steady state case of a 1 m \times 1 m square geometry with cold black walls surrounding a participating media. The governing equation for steady-state, mono-energetic radiative transport is given in Eq. 3.1.²³

$$\Omega \nabla I(\vec{r}, \vec{\Omega}) = \kappa_a \left[I_b(\vec{r}) - I(\vec{r}, \vec{\Omega}) \right] + \sigma_s \left[\frac{1}{4\pi} \int_{4\pi} I(\vec{r}, \vec{\Omega}, t) d\vec{\Omega} - I(\vec{r}, \vec{\Omega}) \right] + S(\vec{r}, \vec{\Omega}) \quad (3.1)$$

By making the substitutions

$$\theta = \frac{T}{T_m} \quad \Psi = \frac{I}{\sigma T_m^4} \quad \vec{\tau} = \frac{\vec{r}}{\|\vec{r}\|}$$

the non-dimensional form of Eq. 3.1 can be written as

$$\Omega \nabla \Psi(\vec{\tau}, \vec{\Omega}) = -\Psi(\vec{\tau}, \vec{\Omega}) + (1 - \omega) \Psi_b(\vec{\tau}, \vec{\Omega}) + \frac{1}{4\pi} \int_{4\pi} \Psi(\vec{\tau}, \vec{\Omega}) d\vec{\Omega} + S(\vec{\tau}, \vec{\Omega}). \quad (3.2)$$

The LBE for Eq. 3.2 is given by²³

$$\Psi(\vec{\tau} + \Delta\tau, \vec{\Omega}) - \Psi(\vec{\tau}, \vec{\Omega}) = \frac{\Delta\tau}{\vec{\Omega}} \left[-\Psi(\vec{\tau}, \vec{\Omega}) + (1 - \omega) \Psi_b(\vec{\tau}, \vec{\Omega}) + \omega w_{\vec{\Omega}} \sum_{i=1}^Q \Psi(\vec{\tau}, \vec{\Omega}_i) \right]. \quad (3.3)$$

DOM solutions are obtained using the commercial code COMSOL. The resulting profiles and contour plots are normalized by the blackbody radiation, I_b .

The profile along the $\tau_y = 0.5$ coordinate was compared for LBM D_2Q_4 and DOM S_2 . Another comparison was done for D_2Q_8 against S_4 . Weights for each LBM lattice are given in Ch. 1. The channel walls are black with emissivities of $\varepsilon = 1$ and are held at a constant dimensionless temperature of 0. The medium was held at a constant dimensionless temperature of unity. For the LBM simulation 200 nodes were used in each direction and the lattice converged within 1,200 iterations. The geometry was discretized using 24,912

domain elements and 400 boundary elements on a finite element mesh.

Fig. 3.1 shows the profiles for LBM and DOM along the centerline for various absorption coefficients, κ . The radiative fields are shown in Fig. 3.2 for D_2Q_4 and S_2 . It can be seen that there is good agreement between the results of both methods.

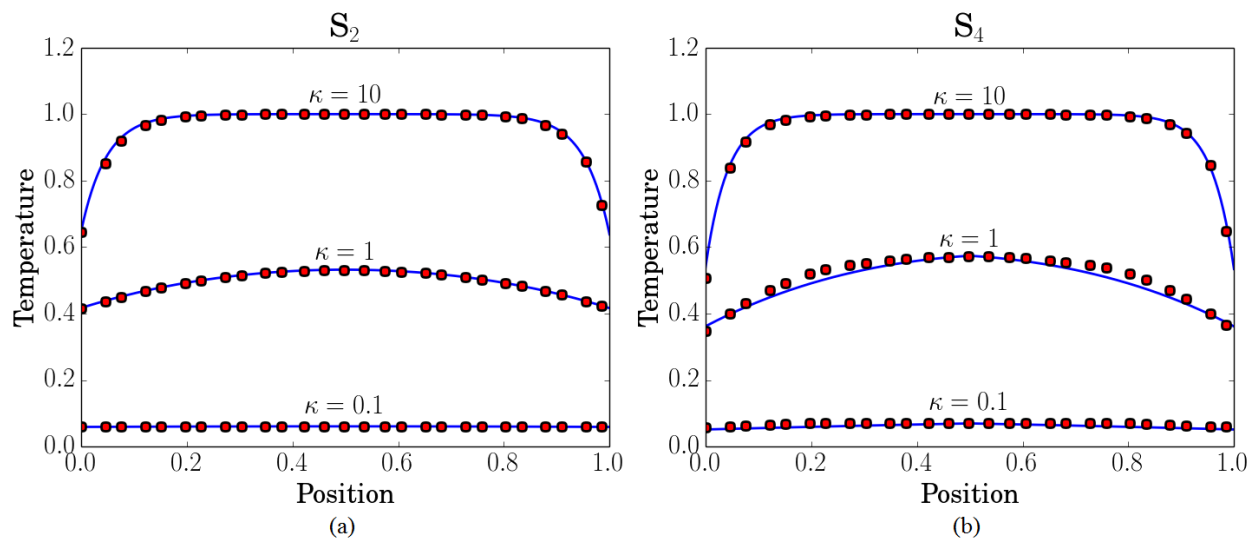


Figure 3.1: Radiative intensity profile along the coordinate $\tau_y = 0.5$ with $\sigma_s = 1$ for (a) D_2Q_4 versus DOM S_2 and (b) D_2Q_8 versus DOM S_4 . $\theta_{wall} = 0$ and $\theta_m = 1$.

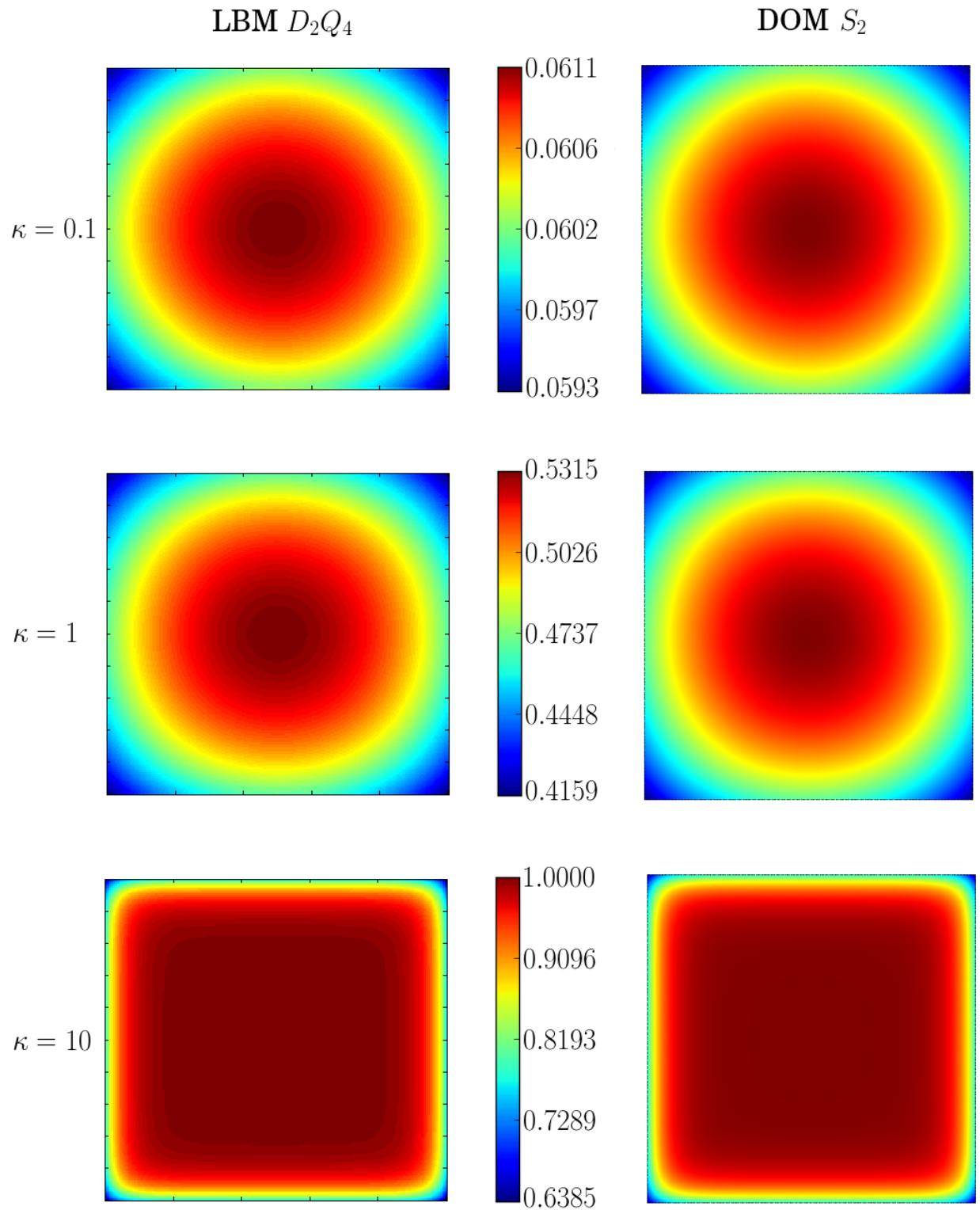


Figure 3.2: Radiative intensity field for $\sigma_s = 1$, $\theta_{wall} = 0$ and $\theta_m = 1$. Maximum absolute relative errors between the profiles are $\varepsilon = 0.0045$, $\varepsilon = 0.0024$ and $\varepsilon = 0.0217$ for $\kappa = 0.01$, $\kappa = 1$ and $\kappa = 10$, respectively.

3.3 Convection-Radiation: Homogeneous Radiative Porous Burner

The high temperature practical applications such as a radiative porous burner involve coupled radiative, conductive and convective heat transfer in a highly complex geometrical configuration. Porous burners are getting increased attention due to their ability to burn very low combustion energy materials or to allow higher degree of thermal mixing. This is achieved by uniform material mixing and allowing the transmission of radiative heat fluxes absorbed by the outer walls, which conduct and convect heat in the axial direction away from the combustion chamber via fluid transport. Accurate and high fidelity modeling of such systems require fully coupled computer simulations of radiative heat transport with conjugate heat transfer in porous media. Talukdar et al. modeled a similar problem in two dimensions using LBM for evaluating the convective flux and Finite Volume Method (FVM) for the radiative flux.³³ In this example a porous media is placed between two plates and fluid is allowed to flow through the media. The geometry and boundary conditions for this problem are shown in Fig. 3.3. Steady state thermal transport with convection, conduction and radiation in two dimensional homogenous porous media is governed by Eq. 3.4.

$$\rho C_p \left(u \frac{\partial T}{\partial x} + v \frac{\partial T}{\partial y} \right) = k \left(\frac{\partial^2 T}{\partial x^2} + \frac{\partial^2 T}{\partial y^2} \right) - \left(\frac{\partial q_r}{\partial x} + \frac{\partial q_r}{\partial y} \right) \quad (3.4)$$

where u and v are velocities parallel and perpendicular to the flow, respectively. In Eq. 3.4, the left-hand side terms are convection terms, and the right-hand side terms represent conduction and radiation heat transfer in the fluid/solid continuum. The radiative heat flux terms are explicitly modeled as

$$\left(\frac{\partial q_r}{\partial x} + \frac{\partial q_r}{\partial y} \right) = \kappa_a \left(\sigma T^4 - \int_{\Omega=4\pi} I(x, y, \vec{\Omega}) d\Omega \right) \quad (3.5)$$

Neglecting the conductive and the radiative heat fluxes in the axial direction (x-direction), and assuming fully developed velocity field yields the non-dimensional form of the governing energy transport equation, Eq. 3.6.³³

$$u \frac{\partial \theta}{\partial \tau_x} = \left(\frac{2}{Pe} \right) \frac{\partial^2 \theta}{\partial \tau_y^2} - \left(\frac{\beta W}{2NPe} \right) \frac{\partial \Psi_r}{\partial \tau_y} \quad (3.6)$$

The left-hand side of Eq. 3.6 is the convection of heat due to the bulk motion of the fluid passing through the channel. It is assumed that the velocity in the transverse direction (y direction) is negligible, thus temperature is only convected axially, or in other words convection is considered only for the x direction. The first term on the right hand side of Eq. 3.6 represents temperature diffusion throughout the media in the transverse direction, where $Pe = \frac{2U_m W \rho C_p}{k}$ is the Peclet number which relates the rate of convection to the rate of diffusion and u_m is the mean axial velocity. It is assumed that in the axial direction diffusion is negligible, thus diffusion is only considered in the transverse direction of thickness W . The dimensionless thicknesses in this example are defined as $\tau_x = \frac{x}{W}$ and $\tau_y = \frac{y}{W}$, and dimensionless axial velocity $u = \frac{u}{u_m}$. The second term on the right-hand side of Eq. 3.6 is the thermal source term due to radiation. The Stark number as defined earlier in previous example is slightly modified to $N = \frac{\beta k}{4\sigma T_R^3}$, where T_R is the reference temperature used to non-dimensionalize the energy equation, and $\Psi_R = \frac{q_r}{\sigma T_R^4}$ is the non-dimensional radiative heat flux. The dimensionless form of radiative heat flux can be simplified to

$$\frac{\partial \Psi_r}{\partial \tau_y} = \beta W (1 - \omega) \left[\theta^4 - \int_{\Omega=4\pi} \psi d\Omega \right] \quad (3.7)$$

where non-dimensional radiation intensity ψ can be obtained from two-dimensional RTE, Eq. 3.8,

$$\mu \frac{\partial \psi}{\partial \tau_x} + \eta \frac{\partial \psi}{\partial \tau_y} = \beta W \left((1 - \omega) \frac{\theta^4}{4\pi} - \psi + \frac{\omega}{4\pi} \int_{\Omega=4\pi} \psi d\Omega \right) \quad (3.8)$$

Eq. 3.8 is similar to the one-dimensional RTE, with the additional term $\eta \frac{\partial \psi}{\partial \tau_y}$, where η is the directional cosine in second dimension. The separate physics of radiative heat transfer in two dimensions was modeled using D_2Q_4 LBM in a previous work¹ for uniform (constant) temperature everywhere in the domain and the results compared well against the S_2 DOM solutions. The LBE equation for Eq. 3.8 with the constant temperature θ_c everywhere in the media can be obtained by re-writing it with dimensionless variables as

$$\psi_i(\tau_x + v_{i,\tau_x} \Delta t, \tau_y + v_{i,\tau_y} \Delta t, t + \Delta t) = \psi_i(\tau_x, \tau_y, t) + \Delta t \beta W \left(w_i (1 - \omega) \theta_c^4 - \psi(\tau_x, \tau_y, t) + \omega w_i \sum_j \psi_j(\tau_x, \tau_y, t) \right) \quad (3.9)$$

Both LBE (D_2Q_4) and DOM (S_2) solutions were relatively less accurate due to use of only four angular directions in two-dimensional planar geometry. As expected in solving the RTE, the accuracy of the solution increases with number of directions. Higher angular resolution results, i.e. the S_4 scheme, agree with the exact solution.³⁴ The S_4 configuration has been shown^{34,35} to be sufficient to capture the radiative heat transfer physics in two-dimensional rectangular or square enclosures. Therefore, Eq. 3.9 was solved with higher angular directions, i.e. the D_2Q_8 lattice configuration, with weights given in the Ch. 1. Similar to other existing LBE algorithms, the problem is solved by explicit time marching which requires the condition $\Delta t \beta < 1$ for stability.

The simplification of the geometry into a homogeneous porous media enables the evaluation of the velocity field analytically. An analytical expression for flow inside a homogeneous porous media was obtained from literature,³⁶ i.e.

$$u(\tau_y, \gamma) = \frac{1 - e^{-2\gamma} - (1 - e^{-\gamma})(e^{\gamma(\tau_y-1)} + e^{-\tau_y\gamma})}{1 - e^{-2\gamma} - 2(1 - e^{-\gamma})^2\gamma^{-1}} \quad (3.10)$$

The fully-developed velocity field is a function of the porosity parameter γ and dimensionless transverse distance, τ_y . For $\gamma \rightarrow 0$, a non-porous media, the velocity profile asymptotically

approaches a laminar Poiseuille flow velocity profile. The velocity field scaled by the maximum Poiseuille flow velocity of 0.1 (for a porosity parameter of $\gamma = 0.1$) is then substituted in the energy equation which can be solved using LBM.

Mishra et al.³⁷ derived LBE to solve material energy equation with radiation term as a source. The radiation source term was computed using collapsed dimension method and then substituted into the LBE form of energy equation. LBE models for convection-diffusion equations with source term have been developed in the past.^{38,39} Based on these existing LBE models for solving convection-diffusion equations with source terms, the LBE form of Eq. 3.6 can be written as Eq. 3.11.

$$\frac{\partial f_i}{\partial t} + \vec{c}_i \cdot \nabla f_i = -\frac{1}{2Pe(c_s^2)^{-1} + 0.5\Delta t} [f_i - f_i^{eq}] + w_i \left(-\frac{\beta W}{2NPe} \nabla \Psi_R \right) \quad (3.11)$$

where the equilibrium function for Eq. 3.11 is given as

$$f_i^{eq} = w_i^m \theta \left[1 + \frac{\vec{c}_i \cdot \vec{u}}{c_s} \right] \quad (3.12)$$

In Eq. 3.12 i is the unit vector in the streaming direction and $c_s = \frac{\Delta \tau_s}{\Delta t}$ is the lattice speed. The D_2Q_4 LBE template with appropriate weights for distribution functions w_i^m as mentioned in the literature³⁸ for convection diffusion equation were used for these computations. Numerical stability is ensured if the factor $(2Pe(c_s^2)^{-1} + 0.5\Delta t)$ was always maintained greater than 0.6, which has been reported by Huang et al.³⁸ to ensure stable convergence for solving convection-diffusion equations with source terms.

The physical example problem, as presented in Fig. 3.3, has two walls maintained initially at higher temperature than the porous medium. These walls dissipate thermal energy into the porous media with fully developed fluid flow via radiative, conductive and convective heat transfer. These computations are performed for $\omega = 0.35$, $N = 0.001$, $Pe = 1600$ and surface wall emissivity of $\varepsilon = 1$. In the case of a non-participating media $\beta = 0$ and radiation does not affect the temperature of the fluid in the channel as there is no absorption

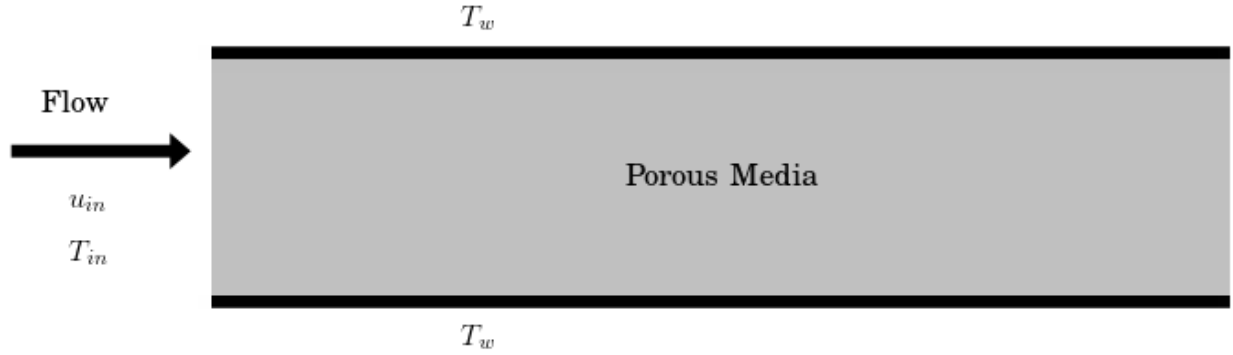


Figure 3.3: *Geometry for the case of a homogeneous porous burner.*

or scattering within the media (Fig. 3.4). For the case of a participating media $\beta = 2$ and radiation emitted from hot walls is absorbed by the homogeneous porous matrix resulting in a higher temperature distribution in the domain. It can be seen in Fig. 3.5 that the radiation interaction causes the entire domain to heat up instantaneously after entering the channel.

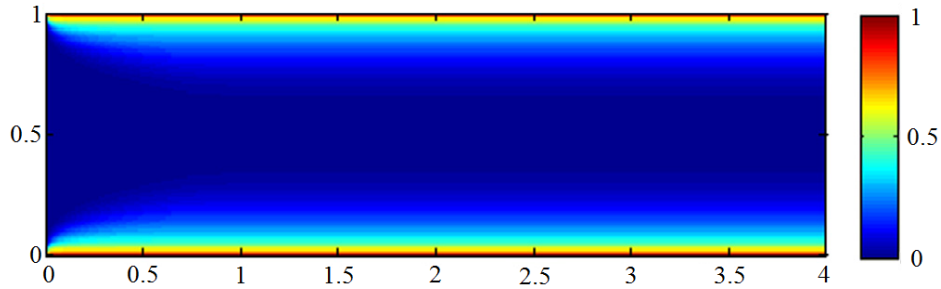


Figure 3.4: *Temperature distribution for the case of a non-participating homogeneous porous media, i.e. without any radiation absorption in the domain.*

Due to the assumption of homogeneity, which allowed the use of a single porosity parameter γ , the approach used in this problem cannot capture differential scattering and absorption in a real porous matrix. Therefore, accurate analysis of thermal transport at high temperatures can only be considered reliable if a heterogeneous medium with anisotropic properties is modeled.

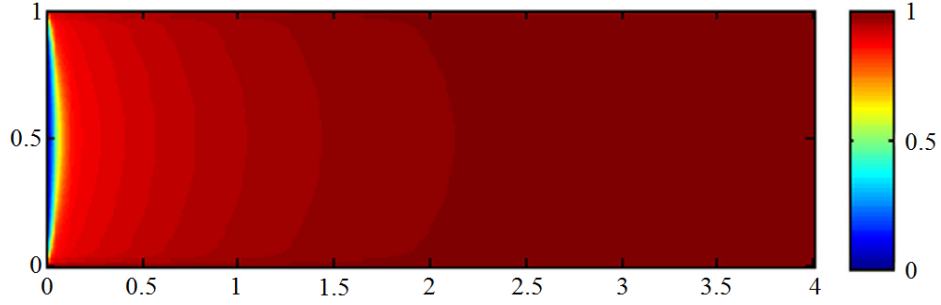


Figure 3.5: *Temperature distribution for the case of a participating homogeneous porous media, i.e. with radiation absorption in the domain.*

3.4 Radiation-Convection: Heterogeneous Radiative Porous Burner

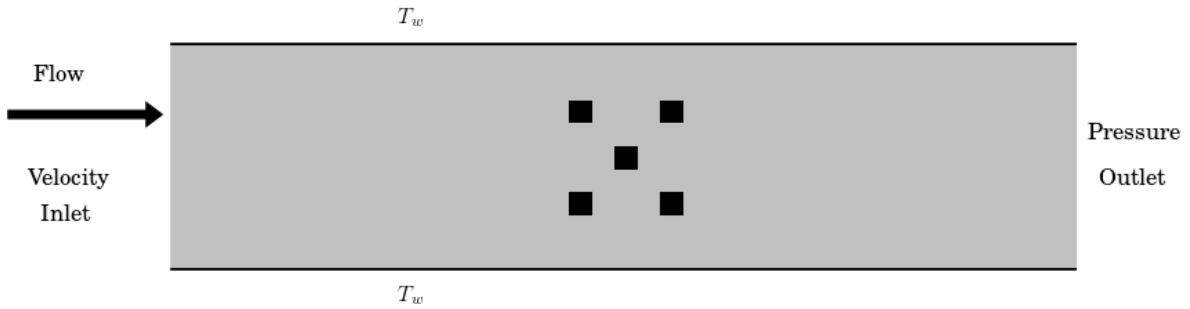


Figure 3.6: *Heterogeneous porous burner with large flow obstacles with different material properties. Size, aspect ratio and grid size are chosen to be exactly the same as the homogeneous case.*

The detailed analysis of radiation-conduction-convection in heterogeneous porous media with realistic void fraction of 30 - 40% and much smaller characteristic dimension of thermal transport as compared to the entire geometry is a computationally challenging task. Moreover, the analytical velocity profile used in the homogeneous case is no longer valid for this heterogeneous region. A simple heterogeneous model with a few solid obstacles is used for the detailed analyses of coupled radiative-conductive-convective heat transfer. The geometry and boundary conditions for this problem are shown in Fig. 3.6. The size of each obstacle is 0.1×0.1 dimensionless units. The velocity field around the obstacles is solved by

LBM and then substituted in energy transport equation. Conduction, convection, and radiation from the walls, obstacles and fluid media were solved simultaneously. In other words all the multi-physics processes involved here are simulated via a fully coupled LBM solver. The fluid flow in the continuum regime is modeled using the non-dimensional steady-state form of the Navier-Stokes equations for incompressible flow with no body force along with the continuity equation⁴⁰

$$\begin{aligned}
u \frac{\partial u}{\partial \tau_x} + v \frac{\partial u}{\partial \tau_y} &= - \frac{\partial p}{\partial \tau_x} + \frac{1}{Re} \left(\frac{\partial^2 u}{\partial \tau_x^2} + \frac{\partial^2 u}{\partial \tau_y^2} \right) \\
u \frac{\partial v}{\partial \tau_x} + v \frac{\partial v}{\partial \tau_y} &= - \frac{\partial p}{\partial \tau_y} + \frac{1}{Re} \left(\frac{\partial^2 v}{\partial \tau_x^2} + \frac{\partial^2 v}{\partial \tau_y^2} \right) \\
\frac{\partial u}{\partial \tau_x} + \frac{\partial v}{\partial \tau_y} &= 0
\end{aligned} \tag{3.13}$$

In these equations u and v are non-dimensional velocities in the τ_x and τ_y directions, respectively, p is non-dimensional pressure, $Re = \frac{2u_m W}{\nu}$ is the Reynolds number and ν is the kinematic viscosity. The LBE's to solve this classical non-dimensional fluid mechanics problem have been developed and presented in multiple references^{24,41}. The most commonly used LBE form for fluid dynamics is

$$\frac{\partial g_k}{\partial t} + \vec{c}_k^f \cdot \nabla g_k = - \frac{1}{2\nu(c_{fs}^2)^{-1} + 0.5\Delta t} [g_k - g_k^{eq}] \tag{3.14}$$

The corresponding equilibrium function for Eq. 3.14 using LBM with the BGK approximation^{16,42,41} is shown in Eq. 3.15.

$$g_k^{eq} = w_k^f \left[1 + \frac{\vec{c}_k^f \cdot \vec{u}}{c_{fs}^2} + \frac{1}{2} \frac{(\vec{c}_k^f \cdot \vec{u})^2}{c_{fs}^4} - \frac{1}{2} \frac{\vec{u}^2}{c_{fs}^2} \right] \tag{3.15}$$

In Eq. 3.15 $c_{fs} = \frac{c_k^f}{\sqrt{3}}$ is the lattice speed, $\vec{c}_k^f = \frac{\Delta \tau_x}{\Delta t} \vec{i} + \frac{\Delta \tau_y}{\Delta t} \vec{j}$ is the unit vector in the streaming direction, w_k^f is the weight of the k -th direction and ρ is density. The standard

D_2Q_9 with weights of $\frac{1}{36}$ for the diagonal directions, $\frac{1}{9}$ for the cardinal directions and $\frac{4}{9}$ for the stationary microscopic velocity²⁴ were used for solving the fluid mechanics problem.

The equation governing the temperature distribution is given by Eq. 3.16.²³

$$u_x \frac{\partial \theta}{\partial \tau_x} + u_y \frac{\partial \theta}{\partial \tau_y} = \frac{2}{Pe} \left(\frac{\partial^2 \theta}{\partial \tau_x^2} + \frac{\partial^2 \theta}{\partial \tau_y^2} \right) - \frac{\beta W}{2NPe} \left(\frac{\partial \Psi_R}{\partial \tau_x} + \frac{\partial \Psi_R}{\partial \tau_y} \right) \quad (3.16)$$

The significance of individual terms in Eq. 3.16 and its LBE form are identical to the homogeneous case and the LBE form of this convection-diffusion equation is identical to the homogeneous case. The radiative heat flux term $\nabla \Psi_R$ is computed using Eq. 3.7-Eq. 3.9 as described before. The fluid mechanics in this problem are not affected by the thermal calculations so this model only presents one-way coupling with the fluid model. The parameters $Re = 100$, $Pe = 1600$ and inlet maximum velocity $u(\tau_x = 0) = 0.1$ are used for these calculations to maintain similarity with the homogeneous case in simulating fluid flow and the role of the convection term in energy transport. The inlet velocity profile was chosen to be Poiseuille flow. The velocity calculations as obtained from the solutions of the LBE (Eq. 3.15) are presented in Fig. 3.7.

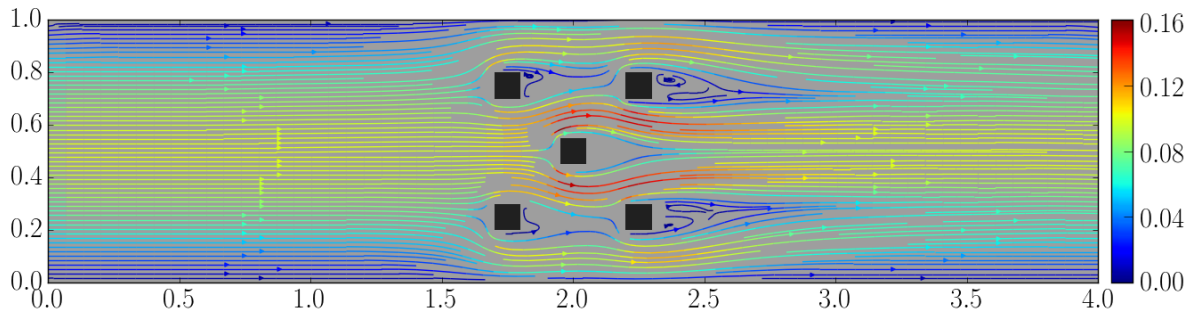


Figure 3.7: Velocity field for flow around the obstacles inside the porous burner, solved with LBM. Colors correspond to the non-dimensional velocity magnitude along the streamline.

After obtaining the velocity field and initialized radiation field, Eq. 3.16 is solved using its LBE form (Eq. 3.11). The temperature and radiative fields are mutually coupled, so they were solved iteratively. The resulting temperature profiles for specific obstacle material

properties of obstacles are shown in Figs. 3.8 and 3.9. The fluid media in both these cases is assumed to absorb negligible radiation. In the first case, the solid obstacles are assumed to be non-absorbers. The results show no temperature change in solids and the fluid near boundaries is hot due to convection near the walls. Due to very high Peclet number, $Pe = 1600$, there is no change in the fluid temperature away from the walls. The second case is modeled with an absorbing and conducting material comprising the obstacles. As fluid is essentially transparent to radiation, the wall radiation instantly starts heating up the obstacles and raising their temperatures. Therefore, the fluid eventually gets heated up from the wall and obstacles both due to convection and conduction.

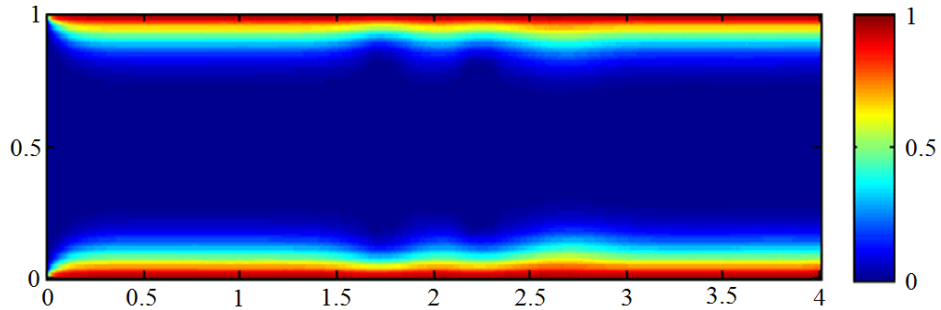


Figure 3.8: *Temperature contour for the entire two dimensional domain with radiatively transparent obstacles ($\beta = 0$).*

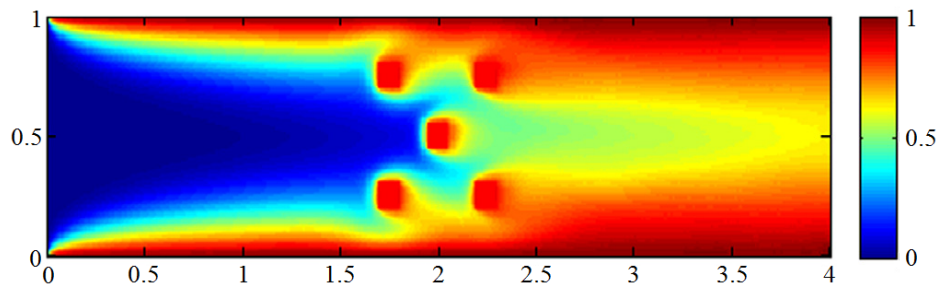


Figure 3.9: *Temperature contour for the entire two dimensional domain with radiatively opaque obstacles ($\beta = 2$ and $N = 0.001$).*

3.5 Conclusions

The LBM based RTE models were extended for their application into coupled multi-physics problems. The results of this work on simple examples in multi-mode heat transfer show that LBM has a potential in solving coupled multi-physics problems. A D_2Q_8 LBE template was used to model radiative transport in a two dimensional square enclosures with constant temperature $\theta_c = 1$ throughout the domain, to check the validity of these LBE templates for solving RTE problems. The results were found to be in good agreement with existing S_4 solutions in the literature.³⁴ A porous radiative burner was modeled using a homogeneous approximation with an analytical velocity field of the fluid stream. The results showed a qualitative effect of the radiation transport in homogeneous participating media. The challenges of this modeling approach were highlighted and an LBM based single-framework approach for solving multi-physics in a heterogeneous model was presented. The fluid transport around the solid obstacles, conduction-convection modeling in the entire domain (solid-fluid) and radiation transport were solved using LBM. A fully coupled LBE model was developed and simulation results were presented for a simplified heterogeneous porous media. The effect of material properties in the entire spatial domain was studied and results were physically interpreted. This work involves only one-way coupling with the fluid model i.e. no feedback is provided to the fluid model based on thermal calculations. However, with this example the LBE approach for modeling the phenomenon of radiative heating of obstacles and in-turn conjugate heating of the fluid stream was demonstrated. Due to its simplified single framework model, LBM is well-suited and has a clear advantage over other deterministic/stochastic numerical techniques for modeling novel mesoscopic applications, such as photo-thermal heating and optical tweezers where fluid motion is directly or indirectly impacted by radiative heat transport. There is, however, significant effort required in the area of LBM based solutions to RTE's prior to its implementation for solving more sophisticated practical problems. One of the important future tasks is to improve the accuracy of the method, i.e. exploring the LBE schemes with higher than first order

accuracy. A second important aspect is to rigorously understand the numerical stability envelopes of using LBE as a single framework for solving multi-physics problems. Finally, extending the LBM for solving multi-energetic RTE's is important to explore its advantages as compared to existing multi-energetic algorithms.

Chapter 4

Nuclear Reactor Criticality

Designing and operating nuclear reactors requires a knowledge of the distribution of neutrons within the reactor. The neutron transport equation (NTE) takes into account the spatio-temporal neutron balance in a nuclear reactor constituted of fissile material. In this chapter LBM is used to solve the NTE to find a reactor configuration (one dimensional) for stable or steady neutron population.

4.1 Chain Reaction

When an atom undergoes fission the result is a combination of fission products and energy. Fission products typically include smaller atoms and neutrons. Reactor materials absorb the excess energy in the form of heat, and the neutron interacts with different nuclei to sustain nuclear reactions.

A fission event can be either spontaneous or induced. Spontaneous fission occurs for heavier nuclei, and typically has a low occurrence for naturally occurring elements. Induced fission is caused by a nucleus absorbing either energy or subatomic particles, which absorption then causes instability in the attractive/repelling forces binding the nucleus together and ultimately results in fission which produces multiple smaller, more stable nuclei. ^{235}U

is an ideal candidate for nuclear reactors because it has a high absorption cross-section and higher fission reaction for neutrons as compared to most of the known elements in nature. Upon absorbing a neutron the nucleus is no longer stable and fissions, resulting in daughter nuclei accompanied by a large emission of energy, typically around 200 MeV. The average number of neutrons emitted per fission, ν , depends on the energy of the neutron whose absorption led to fission. The neutrons emitted from a fission event have different energies, defined by the isotope undergoing fission as well as the energy of the absorbed neutron. A fission neutron energy spectrum, $\chi(E)$, is used to describe the energy of emitted neutrons given an initial incident neutron energy.

4.2 Neutron Transport Equation

The neutron transport equation (NTE) describes the change in neutrons within a volume via balancing the neutrons gained or lost due to various mechanisms. The following derivation of the NTE is given in more detail by Duderstadt and Hamilton²⁶ and can also be found in other introductory texts on nuclear engineering from authors including Lamarsh,⁴³ Shultis and Faw,⁴⁴ and Dunn⁴⁵.

Conceptually the balance of neutrons in a volume, V , can be expressed as

$$\text{Rate of Change of } n = \text{Gains} - \text{Losses}$$

4.2.1 Rate of Change

Assuming the volume does not change with time, the rate of change of neutrons in a volume can be expressed as

$$\int_V \frac{\partial n(\vec{r}, E, \vec{\Omega}, t)}{\partial t} dV \Delta E \Delta \vec{\Omega} \quad (4.1)$$

where $n(\vec{r}, E, \vec{\Omega}, t)$ is the angular neutron density at position \vec{r} with energy E traveling in direction $\vec{\Omega}$ at time t . In order to obtain a number of neutrons from the neutron density it

is necessary to multiply by the range of energy, ΔE , as well as the range of direction $\Delta\vec{\Omega}$, which represent energies and directions in ΔE and $\Delta\vec{\Omega}$ about E and $\vec{\Omega}$.

4.2.2 Gains

The volume gains neutrons through sources such as fission products, neutrons entering the volume, and from scattering from initial energy and/or direction E' and $\vec{\Omega}'$ into the energy and direction of interest, E and $\vec{\Omega}$.

Neutron sources can be expressed as

$$\int_V S(\vec{r}, E, \vec{\Omega}, t) dV \Delta E \Delta\vec{\Omega} \quad (4.2)$$

The source term, S , can be decomposed into two terms: neutrons resulting from fission, S_f , and neutrons from non-fission sources, S_{nf} , such as radioactive elements. Assuming fission neutrons are created instantaneously upon a fission event, and that emission is isotropic, then the number of neutrons created from fission events can be written as

$$\frac{\chi(E)}{4\pi} \int_0^\infty \int_{4\pi} v' \nu(E') \Sigma_f(E') n(\vec{r}, E', \vec{\Omega}', t) d\vec{\Omega}' dE' \quad (4.3)$$

The number of neutrons scattering from energy E' and direction $\vec{\Omega}'$ into energy E and direction $\vec{\Omega}$ is expressed as

$$\int_V v' \Sigma_s(E' \rightarrow E, \vec{\Omega}' \rightarrow \vec{\Omega}) n(\vec{r}, E', \vec{\Omega}', t) dV \Delta E \Delta\vec{\Omega} \quad (4.4)$$

The total number of in-scattered neutrons is the sum of contributions over all energies E' and all directions $\vec{\Omega}'$ given by

$$\int_V \int_0^\infty \int_{4\pi} v' \Sigma_s(E' \rightarrow E, \vec{\Omega}' \rightarrow \vec{\Omega}) n(\vec{r}, E', \vec{\Omega}', t) d\vec{\Omega}' dE' dV \Delta E \Delta\vec{\Omega} \quad (4.5)$$

4.2.3 Losses

Neutrons are lost by neutrons traveling beyond the volume or interacting with the media inside the volume. Interactions result in neutrons either being absorbed or scattered into a different energy and/or direction. The net number of neutrons traveling beyond the boundary of the volume with energy E and direction $\vec{\Omega}$ can be expressed as

$$j(\vec{r}, E, \vec{\Omega}, t) \cdot dS = v\vec{\Omega}n(\vec{r}, E, \vec{\Omega}, t) \cdot dS, \quad (4.6)$$

where j is the neutron current. Using Gauss's Theorem the surface integral (Eq. 4.6) can be converted to a volume integral. Since direction, $\vec{\Omega}$, is independent of position the del operator becomes associative, $\nabla \cdot v\vec{\Omega} = v\vec{\Omega} \cdot \nabla$, and the number of neutrons crossing the surface of the volume becomes

$$\int_V v\vec{\Omega} \cdot \nabla n(\vec{r}, E, \vec{\Omega}, t) dV \Delta E \Delta \vec{\Omega}. \quad (4.7)$$

Neutrons scattering out of ΔE about E and out of $\Delta \vec{\Omega}$ about $\vec{\Omega}$ depends on the total cross section, Σ_t , which is the total cross section for interacting with the media inside the volume and is a combination of the scattering cross section Σ_s and the absorption cross section Σ_a . The resulting expression for scattered neutrons becomes

$$\int_V v\Sigma_t(\vec{r}, E)n(\vec{r}, E, \vec{\Omega}, t) dV \Delta E \Delta \vec{\Omega} \quad (4.8)$$

4.2.4 Neutron Balance

Combining all of the gains and sources results in the integral form of the NTE,

$$\begin{aligned} \int_V \frac{\partial n(\vec{r}, E, \vec{\Omega}, t)}{\partial t} dV \Delta E \Delta \vec{\Omega} &= \int_V \int_0^\infty \int_{4\pi} v \Sigma_s(E' \rightarrow E, \vec{\Omega}' \rightarrow \vec{\Omega}) n(\vec{r}, E, \vec{\Omega}, t) d\vec{\Omega}' dE' dV \Delta E \Delta \vec{\Omega} \\ &+ \int_V S(\vec{r}, E, \vec{\Omega}, t) dV \Delta E \Delta \vec{\Omega} - \int_V v \vec{\Omega} \cdot \nabla n(\vec{r}, E, \vec{\Omega}, t) dV \Delta E \Delta \vec{\Omega} \\ &- \int_V v \Sigma_t n(\vec{r}, E, \vec{\Omega}, t) dV \Delta E \Delta \vec{\Omega} \quad (4.9) \end{aligned}$$

The volume was assumed constant with respect to time, thus the balance of neutrons in the volume, V , becomes

$$\begin{aligned} \frac{\partial n(\vec{r}, E, \vec{\Omega}, t)}{\partial t} &= \int_0^\infty \int_{4\pi} v \Sigma_s(E' \rightarrow E, \vec{\Omega}' \rightarrow \vec{\Omega}) n(\vec{r}, E, \vec{\Omega}, t) d\vec{\Omega}' dE' + S(\vec{r}, E, \vec{\Omega}, t) \\ &- v \vec{\Omega} \cdot \nabla n(\vec{r}, E, \vec{\Omega}, t) - v \Sigma_t n(\vec{r}, E, \vec{\Omega}, t) \quad (4.10) \end{aligned}$$

Using Eq. 4.3 to decompose the source term, the NTE can be rewritten as

$$\begin{aligned} \frac{\partial n(\vec{r}, E, \vec{\Omega}, t)}{\partial t} &= \int_0^\infty \int_{4\pi} v \Sigma_s(E' \rightarrow E, \vec{\Omega}' \rightarrow \vec{\Omega}) n(\vec{r}, E, \vec{\Omega}, t) d\vec{\Omega}' dE' \\ &+ \frac{\chi(E)}{4\pi} \int_0^\infty \int_{4\pi} v' \nu(E') \Sigma_f(E') n(\vec{r}, E', \vec{\Omega}', t) d\vec{\Omega}' dE' + S_{nf}(\vec{r}, E, \vec{\Omega}, t) \\ &- v \vec{\Omega} \cdot \nabla n(\vec{r}, E, \vec{\Omega}, t) - v \Sigma_t n(\vec{r}, E, \vec{\Omega}, t) \quad (4.11) \end{aligned}$$

By defining the angular flux as $\phi = vn(\vec{r}, E, \vec{\Omega}, t)$, where v is velocity and $n(\vec{r}, E, \vec{\Omega}, t)$ is the angular neutron density, the NTE can be written in terms of ϕ as

$$\begin{aligned} \frac{1}{v} \frac{\partial \phi(\vec{r}, E, \vec{\Omega}, t)}{\partial t} = & \int_0^\infty \int_{4\pi} \Sigma_s(E' \rightarrow E, \vec{\Omega}' \rightarrow \vec{\Omega}) \phi(\vec{r}, E, \vec{\Omega}, t) d\vec{\Omega}' dE' \\ & + \frac{\chi(E)}{4\pi} \int_0^\infty \int_{4\pi} \nu(E') \Sigma_f(E') \phi(\vec{r}, E', \vec{\Omega}', t) d\vec{\Omega}' dE' + S_{nf}(\vec{r}, E, \vec{\Omega}, t) \\ & - \vec{\Omega} \cdot \nabla \phi(\vec{r}, E, \vec{\Omega}, t) - \Sigma_t \phi(\vec{r}, E, \vec{\Omega}, t) \quad (4.12) \end{aligned}$$

4.3 Reactor Criticality

4.3.1 Operating Conditions

Nuclear reactors operate on a steady, continuous chain reaction. Reactors are typically comprised of three basic components: 1) fissile fuel containing enriched uranium, 2) a moderator to slow neutrons to the point that they are easily absorbed by the fuel and also to serve as a coolant for the reactor core, and 3) control rods capable of absorbing thermal neutrons that otherwise would have led to fission events. Control rods are typically made from elements with a high neutron affinity such as ^{10}B .

If more neutrons are being created than are being removed the reactor is called supercritical. Conversely, if more neutrons are being removed than are being created the reactor is called subcritical. If the number of created neutrons balances the number of neutrons being removed the reaction is called critical. If the reactor is subcritical external sources must be introduced to sustain the fission events, or the reaction will exponentially decay. If the reactor is supercritical there is an excess of neutrons that are not being used for fission which leads to faster fuel burn up, thus expensive fuel rods need to be replaced more often. If the reactor is supercritical without bound it will cause more reactions and thus more heat which needs to be removed. If the heat cannot be removed the reactor will rise in temperature until physically melting. Thus, the optimum condition for an operating reactor is a

critical condition.

For the case of a critical reactor there is no change in neutrons with respect to time. Typically, at steady state operation the neutron contribution from non-fission sources, S_{nf} , are negligible. These simplifications result in the critical NTE, which balances created and removed neutrons in a reactor, given by

$$\int_0^\infty \int_{4\pi} \Sigma_s(E' \rightarrow E, \vec{\Omega}' \rightarrow \vec{\Omega}) \phi(\vec{r}, E', \vec{\Omega}') d\vec{\Omega}' dE' + \frac{\chi(E)}{4\pi} \int_0^\infty \int_{4\pi} \nu(E') \Sigma_f(E') \phi(\vec{r}, E', \vec{\Omega}') d\vec{\Omega}' dE' = \vec{\Omega} \cdot \nabla \phi(\vec{r}, E, \vec{\Omega}) + \Sigma_t \phi(\vec{r}, E, \vec{\Omega}) \quad (4.13)$$

4.3.2 Eigenvalue Problem

A primary goal in reactor design is to create a reactor capable of critical operation. Since geometry is normally constrained and criticality is desired, the main control factor is the composition of the reactor fuel. Criticality of a given geometry and fuel composition can be determined by solving an eigenvalue problem with the NTE. This is achieved by introducing a scalar, λ , into the fission source term, S_f . With the scalar λ , and assuming negligible non-fission sources, the time-independent critical NTE can be expressed as

$$\frac{\lambda \chi(E)}{4\pi} \int_0^\infty \int_{4\pi} \nu(E') \Sigma_f(E') \phi(\vec{r}, E', \vec{\Omega}') d\vec{\Omega}' dE' = \vec{\Omega} \cdot \nabla \phi(\vec{r}, E, \vec{\Omega}) + \Sigma_t \phi(\vec{r}, E, \vec{\Omega}) - \int_0^\infty \int_{4\pi} \Sigma_s(E' \rightarrow E, \vec{\Omega}' \rightarrow \vec{\Omega}) \phi(\vec{r}, E', \vec{\Omega}') d\vec{\Omega}' dE' \quad (4.14)$$

The fundamental or principle eigenvalue of Eq. 4.14 describes the criticality of the reactor. If $\lambda > 1$ the reactor is subcritical, if $\lambda < 1$ the reactor is supercritical, and if $\lambda = 1$ the reactor is critical. Typically a new variable, the multiplication factor $K_{eff} = \lambda^{-1}$, is defined and used for reactor criticality. K_{eff} has an inverse relation to λ , thus if $K_{eff} > 1$ the reactor is supercritical, if $K_{eff} < 1$ the reactor is subcritical, and if $K_{eff} = 1$ the reactor is

critical.

This work only deals with the one dimensional multi-energetic criticality problems, thus Eq. 4.14 simplifies to

$$\begin{aligned} \mu \frac{\partial \phi(x, E, \mu)}{\partial x} = & \frac{\lambda \chi(E)}{2} \int_0^\infty \int_{-1}^1 \nu(E') \Sigma_f(E') \phi(x, E', \mu') d\mu' dE' \\ & - \Sigma_t \phi(x, E, \mu) + \int_0^\infty \int_{-1}^1 \Sigma_s(E' \rightarrow E, \mu' \rightarrow \mu) \phi(x, E', \mu') d\mu' dE' \end{aligned} \quad (4.15)$$

where, as in Ch. 1, $\mu = \cos \theta$ is a direction cosine, where θ is the elevation angle. The corresponding LBE for Eq. 4.15 is

$$\begin{aligned} \phi(x, E, \mu) = & \phi(x, E, \mu) + w_\mu \frac{dx}{\mu} \left[- \Sigma_t \phi(x, E, \mu) \right. \\ & \left. + \int_0^\infty \int_{-1}^1 \lambda \chi(E) \nu(E') \Sigma_f(E') \phi(x, E', \mu') + \Sigma_s(E' \rightarrow E, \mu' \rightarrow \mu) \phi(x, E', \mu') d\mu' dE' \right] \end{aligned} \quad (4.16)$$

where w_μ is the weight factor for the direction μ .

4.4 Boundary Conditions

Boundary information is required to determine a non-trivial solution for a given reactor configuration. Commonly employed boundary conditions are vacuum, reflected, and periodic. Each of these conditions represent a physical phenomenon, which dictates their use in solving the NTE. Fig. 4.1 shows vacuum, reflected and periodic boundary conditions for the left face of a two dimensional rectangular domain.

4.4.1 Vacuum Boundary Conditions

For a reactor with non-reentrant surfaces the neutrons leaving the surface have no physical way of reentering the reactor. This phenomenon is represented by vacuum boundary

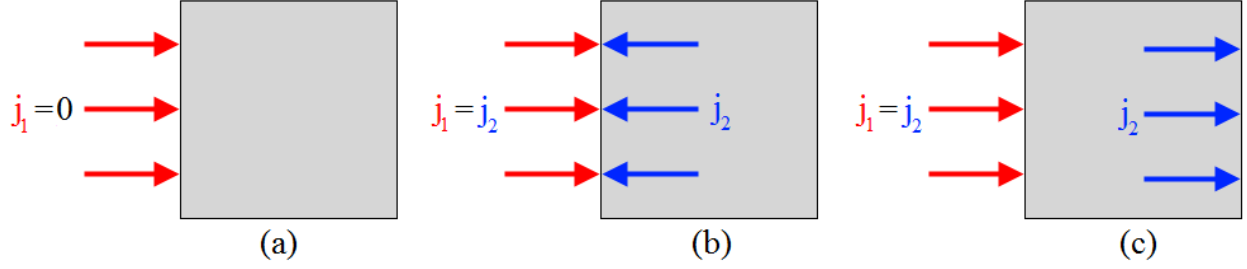


Figure 4.1: A two dimensional domain with (a) vacuum (b) reflected and (c) periodic boundary conditions on a single surface.

conditions which state that there are no incoming neutrons traveling through that surface. Mathematically this is represented as

$$\phi(\vec{r}, E, \vec{\Omega}, t) = 0 \quad \text{for } \vec{\Omega} \cdot \vec{n}(\vec{r}) < 0 \text{ and } \vec{r} \in \partial V \quad (4.17)$$

where $\vec{n}(\vec{r})$ is the unit normal vector to the surface and ∂V is on the boundary of volume V .

4.4.2 Reflected Boundary Conditions

Reflected boundary conditions represent the more realistic scenario of a nuclear reactor where some amount of neutrons are reflected by the moderator. In this case neutrons reenter the surface from which they left. A simplified model implementing reflected boundary conditions would be to let the entering flux be the same as the flux leaving the surface. If the direction of the neutron entering the volume is $\vec{\Omega}$ then the corresponding direction of flux leaving the surface would be $\vec{\Omega}'$ which satisfies the relations $\vec{\Omega} = -\vec{\Omega}'$ and $(\vec{\Omega} \times \vec{\Omega}') \cdot \vec{n}(\vec{r}) = 0$ and the boundary conditions at the surface can be expressed as

$$\phi(\vec{r}, E, \vec{\Omega}, t) = \phi(\vec{r}, E, \vec{\Omega}', t) \quad \text{for } \vec{\Omega} \cdot \vec{n}(\vec{r}) < 0 \text{ and } \vec{r} \in \partial V \quad (4.18)$$

4.4.3 Periodic Boundary Conditions

In a nuclear reactor hundreds of fuel pins are approximately equidistant and nearly symmetrically distributed. Rather than solving for the contribution from each pin simultaneously, a single fuel pin can be simulated with periodic boundary conditions. For periodic boundary conditions whatever leaves one surface enters the opposite surface while retaining the same energy and direction. Given a neutron entering surface 1 with direction $\vec{\Omega}$ then, noting that $\vec{\Omega} = \vec{\Omega}'$, the appropriate boundary value is expressed as

$$\phi(\vec{r}_1, E, \vec{\Omega}, t) = \phi(\vec{r}_2, E, \vec{\Omega}', t) \quad (4.19)$$

where surface 2 is one that satisfies $\vec{n}_1 = -\vec{n}_2$.

4.5 Criticality Condition

4.5.1 Lattice Boltzmann Equation

For mono-energetic, isotropic, steady-state operation with negligible neutron contributions from non-fission sources the eigenvalue criticality equation becomes

$$\vec{\Omega} \cdot \nabla \phi(\vec{r}, \vec{\Omega}) = \frac{\chi}{4\pi K_{eff}} \int_{4\pi} \nu \Sigma_f \phi(\vec{r}, \vec{\Omega}') d\vec{\Omega}' + \int_{4\pi} \Sigma_s \phi(\vec{r}, \vec{\Omega}') d\vec{\Omega}' - \Sigma_t \phi(\vec{r}, \vec{\Omega}) \quad (4.20)$$

For a one dimensional domain the gradient operator becomes $\frac{\partial}{\partial x}$, which is still a partial derivative due to the fact that the angular flux still depends on direction. Assuming a one dimensional domain and introducing the weighted quadrature leads to the LBE for

criticality, which for the i^{th} discrete direction can be expressed as

$$\phi(x + v\Delta t, \vec{\Omega}_i) = \phi(x, \vec{\Omega}_i) + \Delta t \left[w_i \frac{\chi}{K_{eff}} \sum_{i=1}^N \nu \Sigma_f \phi(x, \vec{\Omega}_i) + \sum_{i=1}^N \Sigma_s \phi(x, \vec{\Omega}_i) - \Sigma_t \phi(x, \vec{\Omega}_i) \right]. \quad (4.21)$$

LBM can be used to solve for the criticality in a source iteration manner as described by Duderstadt and Hamilton²⁶ and discussed further in Sec. 4.5.3.

4.5.2 P_1 Method

For some of the benchmark problems where the flux profile values are not given LBM is compared with P_1 methods. Assuming no up-scattering and no thermal neutrons are born from fission, the P_1 equation for neutron flux is given by⁴⁶

$$\frac{d}{dx} \left(-\frac{1}{3\Sigma_t(x, E)} \frac{d\phi(x, E)}{dx} \right) + \Sigma_t(x, E)\phi(x, E) = S(x, E) \quad (4.22)$$

For the thermal flux the source on the right hand side of Eq. 4.22 is comprised of thermalized fast neutrons and self-scattering thermal neutrons. The source for the fast neutrons includes those from fission events and self-scattering.

Classical neutron diffusion theory can be derived from the P_1 approximation by assuming the current is proportional to the neutron concentration such as

$$D = \frac{1}{3\Sigma_t} \quad (4.23)$$

where D is the diffusion coefficient. Using this approximation the one dimensional monoenergetic neutron transport equation in a homogeneous medium with no source term takes the form

$$-D \frac{d^2\phi}{dx^2} + \Sigma_a \phi - \frac{\nu \Sigma_f}{K_{eff}} \phi = 0 \quad (4.24)$$

Various boundary conditions can be applied to diffusion problems. Typically diffusion theory uses Marshak boundary conditions, however LBM uses Mark boundary conditions, thus Mark boundary conditions will be used for neutron diffusion in this work. Mark boundary conditions can be derived by expanding the flux using Legendre polynomials, i.e.

$$\Psi(x, \mu) = \sum_{n=0}^N \frac{d^n \phi(x)}{dx^n} P_n(\mu) \quad (4.25)$$

For a specified flux value on the boundary, and expanding with only two terms, the appropriate boundary condition is given by

$$\Psi_{in}(x, \mu) \approx \frac{1}{2} \phi(x) + \frac{3}{2} \frac{d\phi(x)}{dx} \mu \quad (4.26)$$

where the first two Legendre polynomials are $P_0(\mu) = 1$ and $P_1(\mu) = \mu$. The current on the diffusion boundaries can therefore be expressed as

$$J_{\pm} = \frac{1}{2} \phi + \frac{3}{2} \mu_{\pm} D \frac{d\phi}{dx} \quad (4.27)$$

For non-reentrant boundaries this simplifies to

$$\phi + 3\mu_{\pm} D \frac{d\phi}{dx} = 0 \quad (4.28)$$

By determining the flux through one of the methods discussed in this section the criticality for a specified reactor configuration and composition can be found using the power iteration method.

4.5.3 Power Iteration Method

The power iteration method is a method for iteratively calculating the multiplication factor or critical dimension for a given reactor setup.⁴⁷ First the geometry, initial source due to

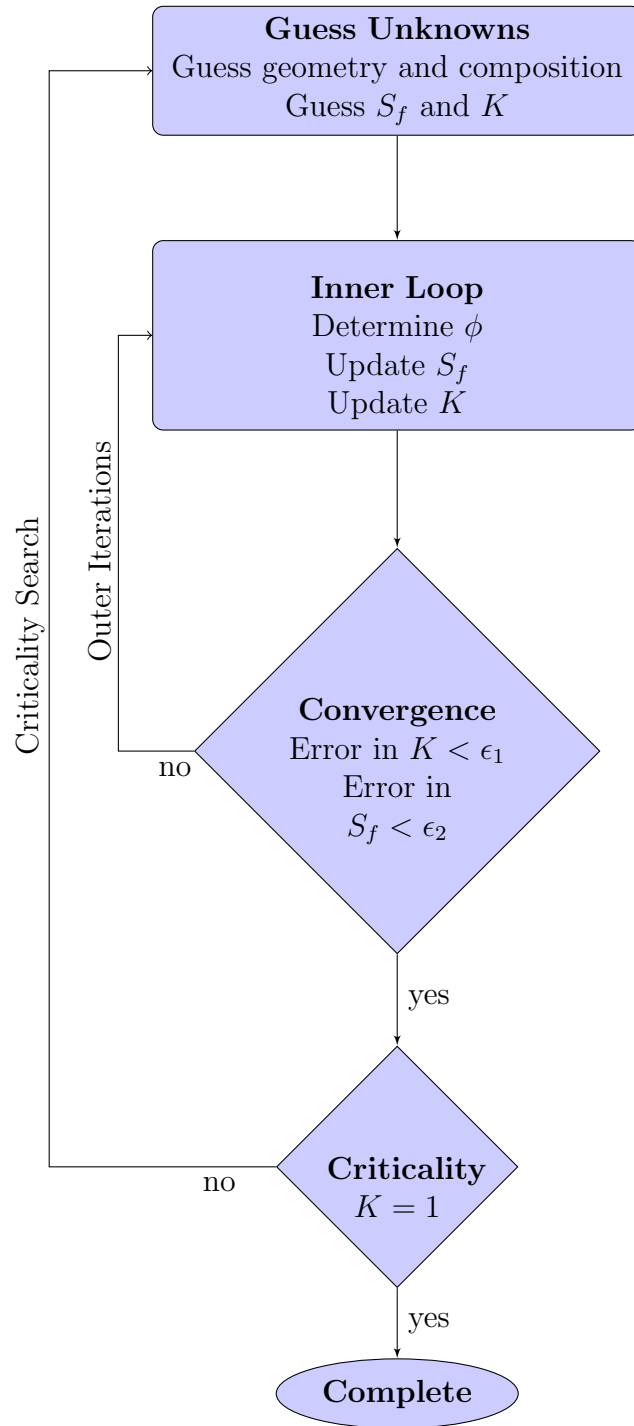


Figure 4.2: Algorithm for the power iteration method.

fission, and multiplication factor are guessed. Flux for each group is calculated at each discretized node. After the flux is calculated the fission source term is updated at each node using Eq. 4.29. Using the new fission source a new multiplication factor is determined by Eq. 4.30.

$$S_f(\vec{r})^{t+1} = \sum_{i=1}^N \nu_i \Sigma_{f_i} \phi_i(\vec{r}) \quad (4.29)$$

$$K^{t+1} \approx K^t \frac{\int S_f^{t+1} d\vec{r}}{\int S_f^t \vec{r}} \quad (4.30)$$

Various convergence criterion can be used, however the most common is to apply a tolerance to the change in fission source and multiplication factor from each iteration, shown mathematically in Eq. 4.31. If both the source and multiplication factor stop changing more than the convergence criterion the solution is assumed to have sufficiently converged.

$$\begin{aligned} \left| \frac{K^t - K^{t-1}}{K^t} \right| &< \epsilon_1 \\ \left| \frac{S^t - S^{t-1}}{S^t} \right| &< \epsilon_2 \end{aligned} \quad (4.31)$$

Criticality is assessed after the solution has converged for a particular reactor setup. Based on the resulting criticality parameters such as reactor dimension or material composition may be adjusted and the entire process repeated until the desired criticality is achieved. The power iteration algorithm is shown in Fig. 4.2.

4.6 Benchmark Problems

The benchmark problems in this chapter are taken from a technical report from Los Alamos National Laboratory.⁴⁸ All of the problems are for a slab reactor with or without cladding and moderator. The critical dimensions are given as $r_c = \frac{\text{slab width}}{2}$ unless otherwise specified. To validate the use of LBM in reactor criticality problems the critical geometry

will be set to the dimensions given in the benchmark report and the eigenvalues, K_{eff} , will be compared.

All of the problems in this chapter are solved with 1000 nodes on a D_2Q_1 lattice. The directional weights are $w_{1,2} = 0.5$. Source and criticality tolerances are $\epsilon_{1,2} = 1 \times 10^{-6}$.

Table 4.1: *One-group macroscopic cross sections.*

Material	ν	Σ_f (cm ⁻¹)	Σ_s (cm ⁻¹)	Σ_t (cm ⁻¹)
Pu (a)	3.24	0.081600	0.225216	0.32640
Pu (b)	2.84	0.081600	0.225216	0.32640
²³⁵ U (a)	2.70	0.065280	0.248064	0.32640
²³⁵ U (b)	2.50	0.069227	0.328042	0.40740
U-D ₂ O	1.70	0.054628	0.464338	0.54628
Fe	0.00	0.000000	0.232094	0.23256
Na	0.00	0.000000	0.086368	0.08636
H ₂ O	0.00	0.000000	0.491652	0.54628

4.6.1 One Group Bare Reactor

Macroscopic cross section data is given in Tab. 4.1 for 1 group reactor materials. For a slab reactor made of material Pu (a) the critical dimension is given as $r_c = 1.853722$ cm. Using this dimension in the LBM code produces $K_{eff} = 0.8050$. For material Pu (b) $r_c = 2.256751$ cm, which yields $K_{eff} = 0.8366$. For a slab reactor made of ²³⁵U (a) the critical dimension is $r_c = 2.872934$ cm, which yields $K_{eff} = 0.8595$. For a bare U-D₂O reactor the critical dimension is $r_c = 10.371065$ cm. Using this dimension with LBM results in $K_{eff} = 0.9946$. Note that the estimate for K_{eff} shows a dependence on the fuel region width. This will be discussed further in the conclusions section.

4.6.2 One Group Reflected Reactor

Using the cross sections given in Tab. 4.1 for U-D₂O with an H₂O reflector, the critical dimension depends on reflector thickness. For core and reflector thicknesses of $r_c = 9.214139$ cm and $t_r = 1.830563$ cm, respectively, $K_{eff} = 0.9992$. For core and reflector thicknesses of $r_c = 8.428096$ cm and $t_r = 18.30563$ cm, respectively, $K_{eff} = 0.9995$.

4.6.3 One Group Reactor with Cladding and Moderator

This benchmark problem involves a non-symmetric reactor configuration. A ²³⁵U (b) reactor core is surrounded by a thin layer of iron cladding. One side is exposed to vacuum conditions, while the opposite side has a sodium moderator. Fuel, cladding and moderator thicknesses are $t_f = 5.120$ cm, $t_c = 0.317$ cm and $t_m = 2.003$ cm, respectively. Note that t_f , the thickness of the fuel, is given as the complete width and not as the critical half-width, r_c . Cross sectional data for each material is given in Tab. 4.1. For this configuration LBM calculated a $K_{eff} = 0.8792$. Diffusion theory with Mark boundary conditions as discussed in Sec. 4.5.2 calculated $K_{eff} = 0.87800$. The resulting flux profiles for diffusion and LBM are shown in Fig. 4.3. A more detailed explanation of applying diffusion theory for this specific problem is provided in the appendix.

4.6.4 Two Group Bare Reactor

This problem involves the criticality of a university research reactor with 93% enriched uranium, ²³⁵U (c). Cross sectional data is given in Tab. 4.2. The critical dimension for the bare slab reactor is given as $r_c = 7.566853$ cm. Using this dimension with LBM results in $K_{eff} = 0.9820$. Fig. 4.4 shows the normalized LBM flux profile compared to the benchmark profile at given slab locations for the ²³⁵U (c) reactor.

For a reactor made of U-D₂O with the cross sectional data from Tab. 4.2 $r_c = 846.632726$ cm. For this configuration LBM yields $K_{eff} = 0.9992$. The number of nodes was increased

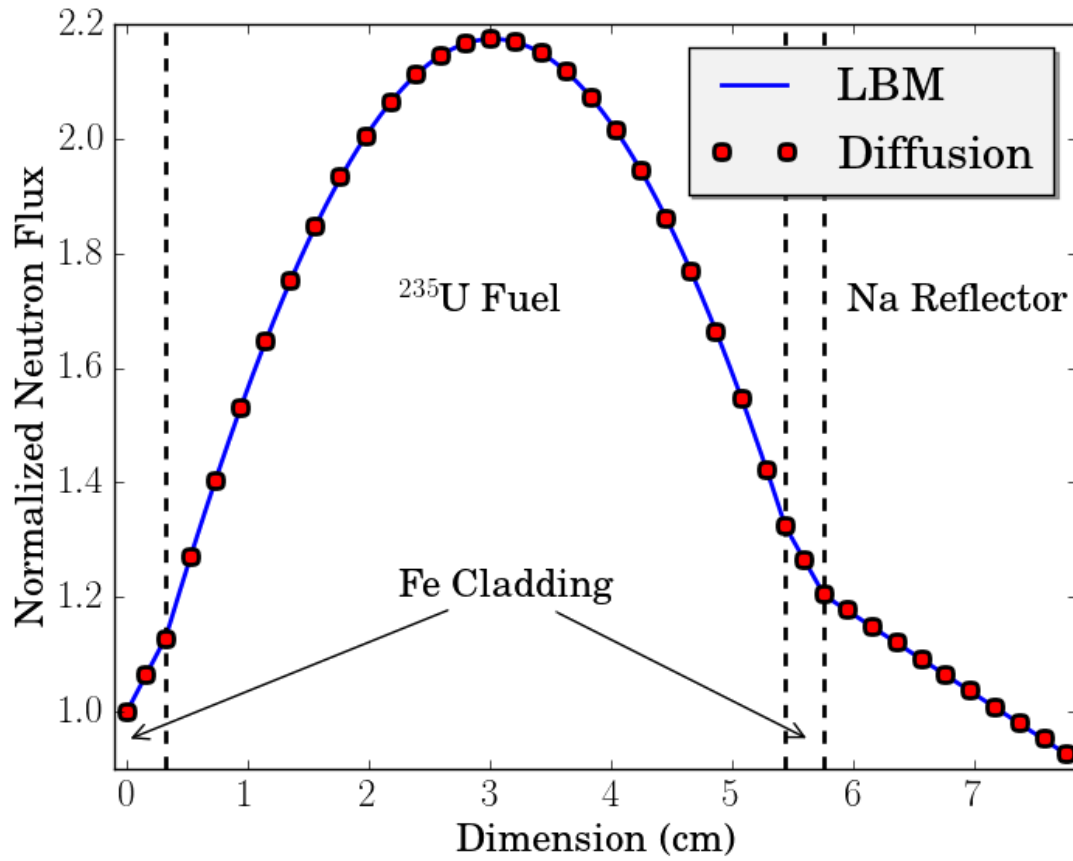


Figure 4.3: Normalized flux profile for the one-group ^{235}U (b) reactor with iron cladding and a sodium moderator using LBM and diffusion theory, both with Mark boundary conditions

Table 4.2: *Two-group macroscopic cross sections.*

Material	ν	Σ_f (cm ⁻¹)	Σ_{ss} (cm ⁻¹)	Σ_{sg} (cm ⁻¹)	Σ_t (cm ⁻¹)	χ
²³⁵ U (c) Fast	2.500	0.001048	0.6256800	0.0292270	0.6569600	1.0
²³⁵ U (c) Thermal	2.500	0.050632	2.4438300	0.0000000	2.5202500	0.0
²³⁵ U (d) Fast	1.004	0.614750	0.0000000	0.0342008	0.6509170	1.0
²³⁵ U (d) Thermal	2.500	0.045704	2.0688000	0.0000000	2.1380000	0.0
²³⁵ U (e) Fast	2.500	0.000836	0.8389200	0.0463500	0.8872100	1.0
²³⁵ U (e) Thermal	2.500	0.029564	2.9183000	0.0007670	2.9727000	0.0
U-D ₂ O Fast	2.500	0.002817	0.3198000	0.0045550	0.3358800	1.0
U-D ₂ O Thermal	2.500	0.097000	0.4241000	0.0000000	0.5462800	0.0
H ₂ O (a) Fast	0.000	0.000000	0.1096742	0.0010005	0.1106832	0.0
H ₂ O (a) Thermal	0.000	0.000000	4.3547000	0.0000000	4.3735000	0.0
H ₂ O (b) Fast	0.000	0.000000	1.2263812	0.1046395	1.3315180	0.0
H ₂ O (b) Thermal	0.000	0.000000	4.3547000	0.0000000	4.3735000	0.0

to 20,000 for this simulation, due to the magnitude of the reactor width.

4.6.5 Two Group Reflected Reactor

The cross sectional data is given in Tab. 4.2 for a ²³⁵U reactor with an H₂O reflector. For a reflector thickness of $t_r = 1.126152$ cm the critical dimension is $r_c = 6.696802$ cm. Using these dimensions with LBM results in $K_{eff} = 0.9912$. For a reflector thickness of $t_r = 5.630757$ cm the critical dimension is $r_c = 4.863392$ cm. Using these dimensions with LBM results in $K_{eff} = 0.9964$.

4.6.6 Two Group Infinite Slab Lattice Cell Reactor

Cross sectional data for the two-group infinite slab lattice reactor made of ²³⁵U (d) and reflected by H₂O (b) is given in Tab. 4.2. For a reflector half-thickness of $t_r = 0.751023$

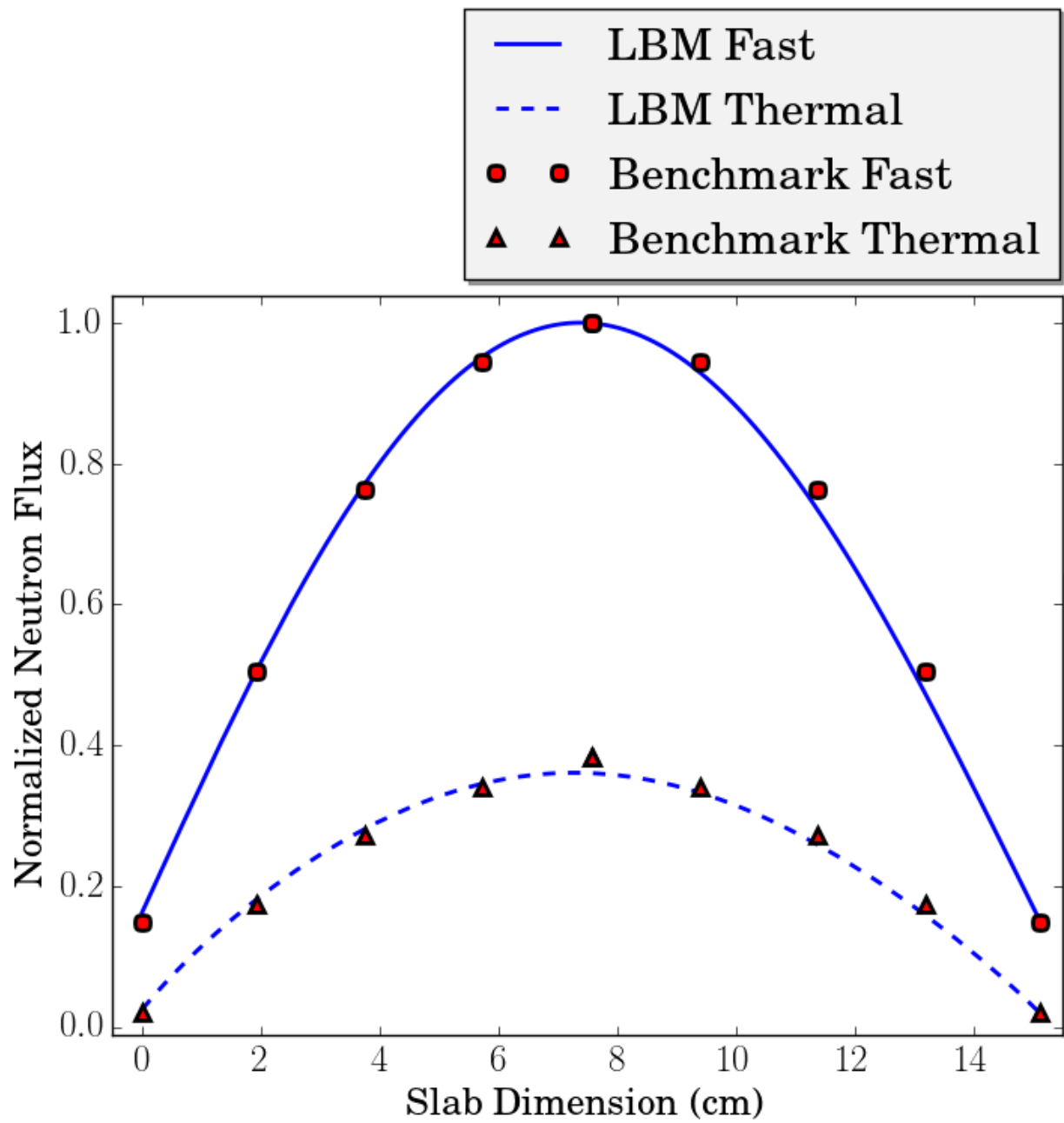


Figure 4.4: Normalized flux profile for the two-group bare research reactor composed of ^{235}U (c).

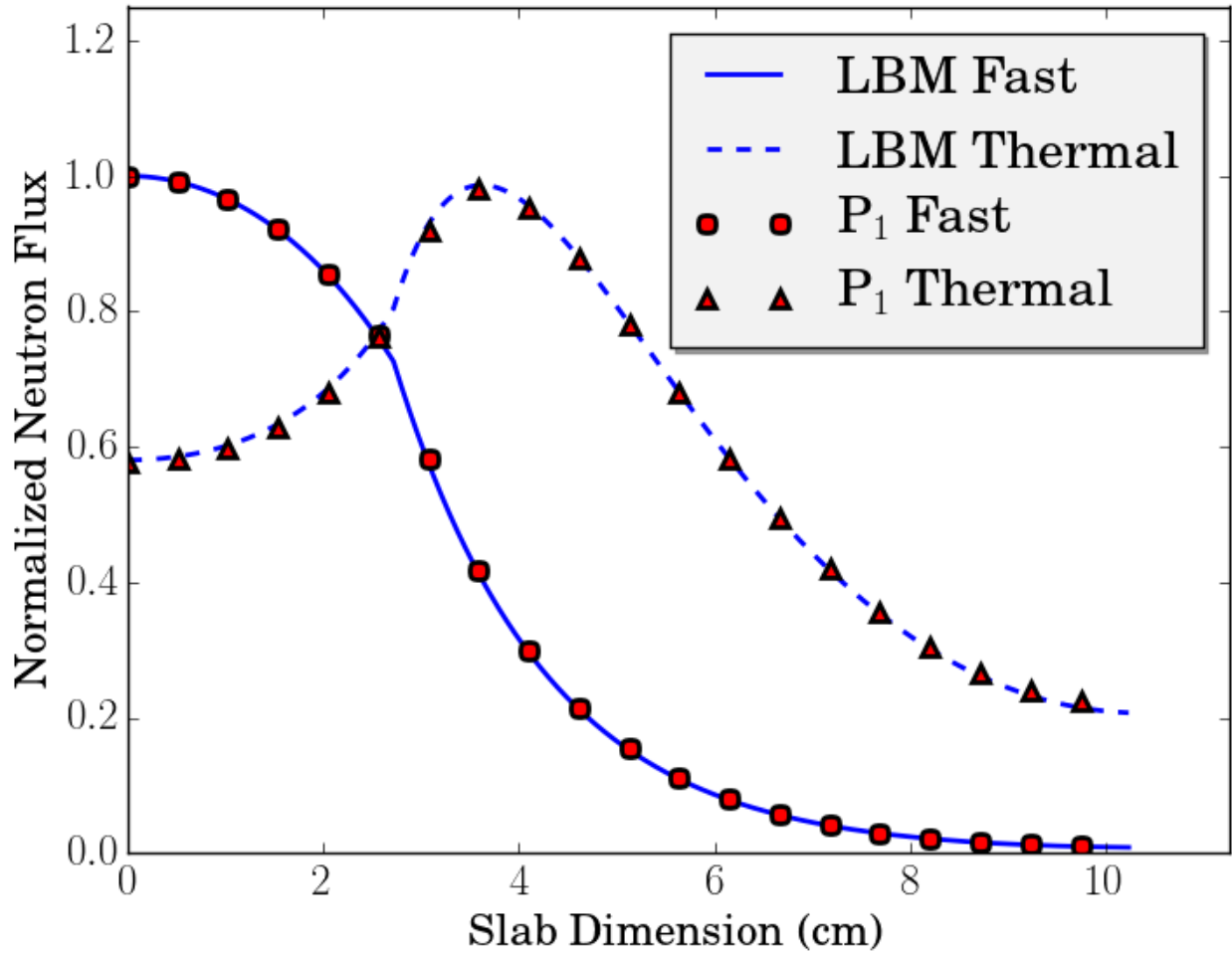


Figure 4.5: Normalized flux profile for the two-group infinite slab lattice cell ^{235}U reactor with $r_c = 2.719087$ cm and $t_r = 7.510225$ cm for both P_1 and LBM methods.

cm the critical dimension is $r_c = 0.341011$ cm. Using these dimensions with LBM results in $K_{eff} = 0.6848$. For a reflector half-thickness of $t_r = 7.510225$ cm the critical dimension is $r_c = 2.719087$ cm. Using these dimensions with LBM results in $K_{eff} = 0.9990$. Fig. 4.5 shows the normalized LBM flux profile for the latter case of the ^{235}U (d) reflected reactor. Fig. 4.5 shows the neutron flux profile, which highlights the effect of a reflector on both fast and thermal fluxes. Fast neutrons are produced in the fuel and not absorbed, but rather travel out of the fuel to the reflector. The reflector has a high cross section for scattering and not for absorption, thus the neutrons collide, losing energy until they are in a thermal energy state. Thus the thermal flux appears to originate in the reflector. Fig. 4.5 shows

excellent agreement between P_1 and LBM methods, as expected based on the discussions in Ch. 2 of this work regarding such a comparison.

4.7 Conclusions

For fuel regions wider than approximately 3 mean free paths (mfp), or for fuel regions with wide reflectors, the results are very agreeable with benchmark values and P_1 methods. The case of thin (fuel width less than approximately 3 mfp) bare reactors show that the fuel width is not sufficiently wide for LBM to accurately predict the reactor criticality. As the fuel width increases the estimate of K_{eff} becomes more accurate. For the case of a reflected reactor thinner fuel regions become less crucial due to the thermal neutron flux being reflected back into the fuel. This is illustrated well in the case of the 2 group infinite slab lattice cell reactor from Sec. 4.6.6, which has reflecting boundary conditions for the thermal neutron flux. In the case of the 1 group reflected and moderated reactor from Sec. 4.6.3 the iron reflector region is too thin, thus neutrons are escaping that should be returning to the reactor. The results indicate that in this case, if the reflector region was increased then criticality could be more accurately represented by LBM. The problems in this chapter show the capability of LBM to solve reactor criticality eigenvalue problems. Results compare well with literature and benchmark problems for sufficiently thick fuel and reflector regions.

Chapter 5

Conclusions and Future Work

5.1 Conclusions

It was shown in Ch. 2 that LBM is well suited for solving coupled non-equilibrium radiative transport problems with participating media. For the case of a linearized set of coupled differential equations representing energy and radiation, results showed that LBM compares well with the semi-analytical solutions. This one dimensional algorithm was further extended for the case of non-linearly coupled energy and radiation transport equations and results showed good agreement with P_1 methods for wall emissivities from $\varepsilon = 0$ to $\varepsilon = 1$ and Stark number parameters from $N = 0.01$ to $N = 10$. The error analysis was done and shown to be a first-order accurate method.

The two dimensional LBM lattice configurations were derived for isotropic transport. The LBM results from D_2Q_4 and D_2Q_8 configurations were compared to DOM configurations of S_2 and S_4 , respectively, for the case of a participating media with a constant non-dimensional temperature of $\theta_m = 1$ surrounded by cold black walls. Results showed good agreement, especially when the number of discrete directions were exactly equal in both methods.

One of the goals of this work was to extend the application of LBM to coupled modeling

of radiation and material energy transport. Two dimensional porous burners were used to demonstrate this coupled modeling. The case of a homogeneous porous burner was used to illustrate the effects of having a participating or a non-participating media. An analytical velocity profile was used to represent fluid flow in the porous media based on a porosity parameter, γ . The results showed that for the case of a participating porous media the fluid heated up almost immediately upon entering the channel, whereas for the case of a non-participating media the fluid only heated up very close to the hot walls. To capture a more realistic application of LBM to radiative transfer a heterogeneous porous burner was considered in which detailed modeling of conjugate heat transfer was conducted using LBM. The Navier-Stokes equations for incompressible flow with no body force along with the continuity equation were solved using LBM. The resulting velocity field was used to calculate the energy equation with LBM, which considered thermal contributions via convection, conduction and radiation. The radiative field was solved for with LBM. Due to the dependence of the energy and radiation equations the coupled equations were solved iteratively. The cases of non-participating and participating obstacles were considered. For the case of non-participating obstacles the fluid heated near the walls due to convection, however because of the high Peclet number the fluid did not change considerably away from the walls, thus the solid obstacles did not rise in temperature. For the case of participating obstacles the solid obstacles absorbed radiation and heated up, which heated the fluid due to convection from the surface of the obstacles. The application of LBM to a heterogeneous porous burner showed the capability of LBM to solve coupled multi-physics simulations including fluid, temperature and radiation interactions. While this problem included one-way fluid and energy coupling, an additional term could readily be added to fully couple the fluid and energy equations thus incorporating buoyancy effects due to thermal gradients.

Chapter 4 showed the application of LBM to neutron criticality problems in a one dimensional slab geometry. The well-known source iteration method described by Duderstadt²⁶ was adopted for LBM to obtain critical slab dimensions for various benchmarked compo-

sitions. Results showed very good agreement between LBM and the reported benchmark values as well as with P_1 methods for multi-group flux profiles. LBM produced very good results for sufficiently thick (> 4 mfp) slab reactors. Two-group flux profiles of bare and reflected reactor configurations matched very well with reported values and with P_1 profiles.

5.2 Future Work

The most immediate work to be done is to extend the application of LBM for radiative transport into realistic three dimensional domains. This includes deriving the directional weights for three dimensional isotropic lattices such that the macroscopic variables are conserved and the local physics are accurately balanced.

There is little room to adopt a polar angle in one and two dimensional cases due to fixed lattice configurations, which limits the accuracy of LBM for some cases. The effect of azimuthal variation in one dimension and the effect of polar angle variation in two dimensions is necessary to improve the accuracy of the method. For example, this will enable the LBM based solution of thin slabs. Another limitation with the current formulation is that discrete LBEs are only first order accurate with respect to spatial grids. The solution can be enhanced by using more nodes to discretize the domain, but this becomes exponentially expensive with added dimensions. Adaptive mesh refinement (AMR) has been used in LBM applications for fluid simulations to dynamically address the allocation of computational resources during run time. With AMR regions of interest, such as on interfaces or areas with high concentrations, are discretized with a finer mesh using a higher node density while areas that are not of particular interest are discretized with a coarser mesh using a lower node density. This saves computational resources, but does not fully address the problem of first order accuracy thus higher order accurate LBEs must be derived for solving larger domain problems. The second order accurate method for radiation transport will be conveniently coupled to the second order method for advection-diffusion and fluid transport

problems, and the second order of accuracy for the coupled system can be preserved.

Bibliography

- [1] H. Bindra and D. V. Patil. Radiative or neutron transport modeling using a lattice boltzmann equation framework. *Phys. Rev. E*, 86, 2012.
- [2] <http://detexify.kirelabs.org/classify.html>.
- [3] J. B. Casady and R. W. Johnson. Status of silicon carbide (sic) as a wide-bandgap semiconductor for high-temperature applications: A review. *Solid State Electron.*, 1996.
- [4] M. W. Barsoum, D. Brodtkin, and T. El-Raghy. Layered machinable ceramics for high temperature applications. *Scr. Mater.*, 1997.
- [5] Y. Enomoto and S. Furuhashi. A study of the local heat transfer coefficient on the combustion chamber walls of a four-stroke gasoline engine. *J. Soc. Mech. Eng.*, 32: 107–114, 1989.
- [6] C. Tang, Y. Tang, J. Zhu, Y. Zou, J. Li, and X. Ni. Design and manufacture of the fuel element for the 10 mw high temperature gas-cooled reactor. *Nucl. Eng. Des.*, 218: 91–102, 2002.
- [7] F. R. Knapp, S. Mirzadeh, A. Beets, M. O’Doherty, P. Blower, E. Verdera, J. Gaudiano, J. Kropp, J. Guhlke, H. Palmedo, and H. Biersack. Reactor-produced radioisotopes from ornl for bone pain palliation. *Appl. Radiat. Isot.*, 49:309–315, 1998.
- [8] D. S. McGregor, Z. He, H. A. Seifert, D. K. Wehe, and R. A. Rojas. Single charge carrier type sensing with a parallel strip pseudo-frisch-grid cdznte semiconductor radiation detector. *Appl. Phys. Lett.*, 72, 1998.

- [9] F. P. Incropera, D. P. DeWitt, T. L. Bergman, and A. S. Lavine. *Fundamentals of Heat and Mass Transfer*, volume 5th Ed. Hoboken: Wiley, 2006.
- [10] P. Asinari, S. Mishra, and R. Borchiellini. A lattice boltzmann formulation to the analysis of radiative heat transfer problems in a participating media. *Numer. Heat Transfer, Part B*, 2010.
- [11] Y. Ma, S. Dong, and H. Tan. Lattice boltzmann method for one-dimensional radiation transfer. *Phys. Rev. E*, 84, 2011.
- [12] J. Hardy, O. de Pazzis, and Y. Pomeau. Time evolution of a two-dimensional classical lattice system. *Phys. Rev. Lett.*, 13:1042, 1973.
- [13] A. A. Mohamad. *Lattice Boltzmann Method Fundamentals and Engineering Applications with Computer Codes*. New York: Springer, 2011.
- [14] Z. Guo and C. Shu. *Lattice Boltzmann Method and its Applications in Engineering*. Hackensack: World Scientific, 2013.
- [15] F. Kuznik, C. Obrecht, G. Rusaouen, and J. Roux. Lbm based flow simulation using gpu computing processor. *Computers and Mathematics with Applications*, 59:2380–2392, 2010.
- [16] P. L. Bhatnagar, E. P. Gross, and M. Krook. A model for collision processes in gases i: small amplitude processes in charged and neutral one-component systems. 94:511–525, 1954.
- [17] G. R. McNamara and G. Zanetti. Use of the boltzmann equation to simulate lattice gas automata. *Phys. Rev. Lett.*, 61:2332–2335, 1988.
- [18] F. Higuera and J. Jimenez. Boltzmann approach to lattice gas simulations. *Europhys. Lett.*, 9:663–668, 1989.

- [19] S. Chen, H. Chen, D. O. Martinez, and W. H. Matthaeus. Lattice boltzmann model for simulation of magnetohydrodynamics. *Phys. Rev. Lett.*, 67:3776–3779, 1991.
- [20] J. Koelman. A simple lattice boltzmann scheme for navier-stokes fluid flow. *Europhys. Lett.*, 15:603–607, 1991.
- [21] Y. H. Qian, D. d’Humières, and P. Lallemand. Lattice bgk models for the navier-stokes equation. *Europhys. Lett.*, 17:479–484, 1992.
- [22] L. Boltzmann. Weitere studien über das wärmeleichgewicht unter gasmolekülen. *Sitzungsberichte Akademie der Wissenschaften*, 66:275–370, 1872.
- [23] R. McCulloch and H. Bindra. Coupled radiative and conjugate heat transfer in participating media using lattice boltzmann methods. *Comput. Fluids*, 2015. (Accepted).
- [24] D. A. Wolf-Gladrow. *Lattice-Gas Cellular Automata and Lattice Boltzmann Models - An Introduction*. New York: Springer, 2005.
- [25] H. Jeffreys. *Cartesian Tensors*. Cambridge: Cambridge University Press, 1965.
- [26] J. Duderstadt and L. Hamilton. *Nuclear Reactor Analysis*. New York: John Wiley and Sons, 1976.
- [27] X. He, S. Chen, and G. D. Doolen. A novel thermal model for the lattice boltzmann method in incompressible limit. *J. Comput. Phys.*, 146:282–300, 1998.
- [28] Z. L. Guo and C. G. Zheng. A coupled lattice bgk model for the boussinesq equations. *Int. J. Numer. Meth. Fluids*, 39:325–342, 2002.
- [29] B. Su and G. L. Olson. An analytical benchmark for non-equilibrium radiative transfer in an isotropically scattering medium. *Ann. Nucl. Energy*, 24:1035–1055, 1997.
- [30] B. D. Ganapol and G. C. Pomraning. The non-equilibrium marshak wave problem: A transport theory solution. *J. Quant. Spectrosc. Radiat. Transfer*, 29:311–320, 1983.

- [31] M. Modest. *Radiative Heat Transfer*, volume 3rd Ed. New York: Academic Press, 2013.
- [32] E. E. Lewis and W. F. Miller. *Computational Methods of Neutron Transport*. Wiley-Interscience, 1993.
- [33] P. Talukdar, S. Mishra, D. Trimis, and F. Durst. Combined radiation and convection heat transfer in a porous channel bounded by isothermal parallel plates. *Int. J. Heat Mass Transfer*, 47:1001–1013, 2004.
- [34] J. S. Truelove. Discrete ordinate solutions of the radiative transport equation. *J. Heat Transfer*, 109, 1987.
- [35] W. A. Fiveland. Discrete ordinate solutions of the radiative transport equation for rectangular enclosures. *J. Heat Transfer*, 106, 1984.
- [36] M. Kaviany. Laminar flow through a porous channel bounded by isothermal parallel plates. *International Journal of Heat and Mass Transfer*, 28:851–858, 1985.
- [37] S. Mishra, A. Lankadasu, and K. Beronov. Application of the lattice boltzmann method for solving the energy equation of a 2d transient conduction radiation problem. *Int. J. Heat Mass Transfer*, 48, 2005.
- [38] H. Huang, X. Liu, and M. Sukop. Numerical study of lattice boltzmann methods for a convection-diffusion equation coupled with navier-stokes equations. *J. Phys. A: Math Theory*, 44, 2011.
- [39] B. Chopard, J. Falcone, and J. Latt. The lattice boltzmann advection-diffusion model revisited. *Eur. Phys. J. Spec. Top.*, 171, 2009.
- [40] F. White. *Fluid Mechanics*. McGraw Hill, 7th edition, 2011.
- [41] X. He and L. Luo. Theory of the lattice boltzmann method: From the boltzmann equation to the lattice boltzmann equation. *Phys. Rev. E*, 56, 1997.

- [42] C. Aidun and J. Clausen. Lattice boltzmann method for complex flows. *Annu. Rev. Fluid Mech.*, 42, 2010.
- [43] J. R. Lamarsh. *Introduction to Nuclear Engineering*, volume 2nd Ed. Reading: Addison-Wesley, 1983.
- [44] J. K. Shultis and R. E. Faw. *Radiation Shielding*. La Grange Park: American Nuclear Society, 2000.
- [45] W. L. Dunn and J. K. Shultis. *Exploring Monte Carlo Methods*. New York: Academic Press, 2012.
- [46] Weston M. Stacey. *Nuclear Reactor Physics*. Wiley-VCH, 2nd edition, 2007.
- [47] F. Scheben. *Iterative Methods for Criticality Computations in Neutron Transport Theory*. PhD thesis, University of Bath, 2011.
- [48] A. Sood, R. A. Forster, and D. K. Parsons. Analytical benchmark test set for criticality code verification. Technical report, Los Alamos National Laboratory, 1999.

Appendix A

Example Codes

A.1 2D LBM Code

This example code determines the steady state radiative field in a square of length $L=1$. The $x = 0$ face has a specified non-dimensional radiative flux of 1 and a constant source of strength 0.5 is present throughout the media. Neumann boundary conditions are applied to the remaining faces of the square. The media is non-scattering. Fig. [A.1](#) shows the radiative field. Fig. [A.2](#) shows the radiative flux profile along the centerline of the medium normal to the face with the specified radiative flux.

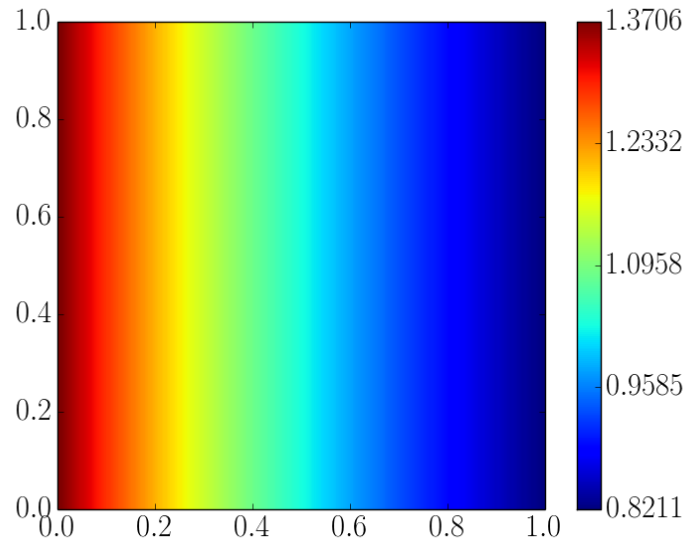


Figure A.1: *Radiative field strength throughout the medium.*

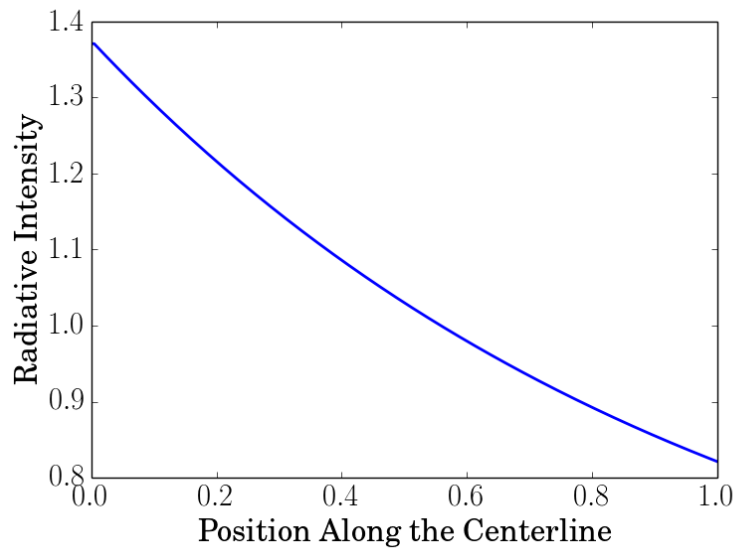


Figure A.2: *Radiative field strength along the centerline $y = 0.5$.*


```

1 % SOLVING FOR A RADIATIVE FIELD USING THE LATTICE BOLTZMANN METHOD.
2 %
3 % This program calculates the steady state radiative field in a square
4 % of length L. The left face has a specified radiative flux of 1 and a
5 % constant source of strength 0.5 is present throughout the media.
6 % Neumann boundary conditions are applied to the remaining faces of the
7 % square. The media is non-scattering.
8 %
9 % Author: Richard McCulloch
10 % Date: 17 Feb 2015
11
12 clear all
13 close all
14 clc
15
16 Q=4; % Number of directions
17 N=100; % Number of nodes in each direction
18 x=linspace(0,1,N); % Optical thickness matrix
19 L=1; % Total optical thickness
20 dx=L/(N-1); % Node spacing
21 w=0.25; % Directional weight factors
22 f=zeros(N,N,Q); % Distribution matrix
23 fL=1; % Boundary flux value
24 S=0.5; % Uniform source strength
25 err=1; % Error variable
26 tol=1E-10; % Convergence tolerance
27
28 while(err>tol)
29 % Store the previous solution
30 fold=f;
31
32 % Boundary Conditions
33 f(1, :, 1)=fL; % Dirichlet bc on Left Wall
34 f(N, :, 3)=f(N-1, :, 3); % Neumann bc on Right Wall
35 f(:, 1, 2)=f(:, 2, 2); % Neumann bc on Bottom Wall
36 f(:, N, 4)=f(:, N-1, 4); % Neumann bc on Top Wall
37
38 % Colliding
39 f=f-dx.*(f-w*S);
40
41 % Streaming
42 f(2:N, :, 1)=f(1:N-1, :, 1); % Direction 1 streams to the right
43 f(:, 2:N, 2)=f(:, 1:N-1, 2); % Direction 2 streams to the top
44 f(1:N-1, :, 3)=f(2:N, :, 3); % Direction 3 streams to the left
45 f(:, 1:N-1, 4)=f(:, 2:N, 4); % Direction 4 streams to the bottom
46
47 % Compute the maximum error by the change in f
48 err=max(max(max(abs((f-fold)./f))));
49 end
50
51 % Plot the results
52 figure
53 imagesc(x, x, sum(f, 3))
54 daspect([1 1 1])
55 colorbar
56 xlabel('X')
57 ylabel('Y')
58 title('LBM D2Q4')

```

Listing A.1: Matlab D_2Q_4 code.

```

1  /* SOLVING FOR A RADIATIVE FIELD USING THE LATTICE BOLTZMANN METHOD.
2  *
3  * This program calculates the steady state radiative field in a square
4  * of length L. The left face has a specified radiative flux of 1 and a
5  * constant source of strength 0.5 is present throughout the media.
6  * Neumann boundary conditions are applied to the remaining faces of the
7  * square. The media is non-scattering.
8  *
9  * Author: Richard McCulloch
10 * Date: 17 Feb 2015
11 */
12
13 #include<iostream> // cout
14 #include<fstream> // ofstream
15 #include<cmath> // fabs
16 using namespace std;
17
18 int main(){
19     int Nx=100, // Number of nodes in the x direction
20         Ny=100, // Number of nodes in the y direction
21         Q=4; // Number of directions
22     double f[100][100][4]={0.0}, // Distribution matrix
23            fold[100][100][4], // Previous distribution matrix
24            fL=1.0, // Boundary flux value
25            err=1.0, // Error variable
26            tol=1.0E-10, // Convergence tolerance
27            L=1.0, // Total optical thickness
28            dx=L/(Nx-1.0), // Node spacing
29            S=0.5, // Uniform source strength
30            w=0.25, // Directional weight factors
31            temp; // Temporary variable
32
33     while(err > tol){
34         // Store previous solution
35         for(int j=0; j<Ny; j++){
36             for(int i=0; i<Nx; i++){
37                 for(int k=0; k<Q; k++){
38                     fold[i][j][k]=f[i][j][k];
39                 }
40             }
41             // Boundary Conditions
42             for(int j=0; j<Ny; j++){
43                 f[0][j][0]=fL; // Dirichlet BC on Left Wall
44                 f[Nx-1][j][2]=f[Nx-2][j][2]; // Neumann BC on Right Wall
45             }
46             for(int i=0; i<Nx; i++){
47                 f[i][0][1]=f[i][1][1]; // Neumann BC on Bottom Wall
48                 f[i][Ny-1][3]=f[i][Ny-2][3]; // Neumann BC on Top Wall
49             }
50             // Colliding
51             for(int j=0; j<Ny; j++){
52                 for(int i=0; i<Nx; i++){
53                     for(int k=0; k<Q; k++){
54                         f[i][j][k]=f[i][j][k]-dx*(f[i][j][k]-w*S);
55                     }
56                 }
57             }
58             // Streaming
59             for(int j=0; j<Ny; j++){
60                 for(int i=0; i<Nx-1; i++){
61                     f[Nx-i-1][j][0]=f[Nx-i-2][j][0];
62                     f[i][j][2]=f[i+1][j][2];
63                 }
64             }
65             for(int j=0; j<Ny-1; j++){
66                 for(int i=0; i<Nx; i++){

```

```

65         f[i][Ny-j-1][1]=f[i][Ny-j-2][1];
66         f[i][j][3]=f[i][j+1][3];
67     }
68
69     // Compute the maximum error by the change in f
70     err=0.0;
71     for(int j=0; j<Ny; j++){
72         for(int i=0; i<Nx; i++){
73             for(int k=0; k<Q; k++){
74                 temp=fabs((f[i][j][k]-fold[i][j][k])/(f[i][j][k]));
75                 if(temp > err)
76                     err=temp;
77             }
78         }
79
80     // Output the results for post-processing
81     ofstream output("lbm_output.dat");
82     for(int j=0; j<Ny; j++){
83         for(int i=0; i<Nx; i++){
84             output << f[i][j][0]+f[i][j][1]+f[i][j][2]+f[i][j][3] << " ";
85             output << endl;
86         }
87     }
88     return 0;
89 }

```

Listing A.2: *C++ D_2Q_4 code.*

A.2 1D Criticality Code

This code solves for the critical eigenvalue of a bare 1 group U-D₂O reactor using LBM.

```
1 % This code solves the eigenvalue criticality problem for a bare 1
2 % dimensional slab reactor made of U-D2O.
3 %
4 % Author: Richard McCulloch
5 % Date: 5 March 2015
6
7 clear all; close all; clc
8
9 nu=1.70; % Average number of neutrons emitted per fission event
10 Sigma_f=0.054628; % Macroscopic cross section for fission
11 Sigma_s=0.464338; % Macroscopic cross section for scatter
12 Sigma_t=0.54628; % Macroscopic total cross section
13 L=2*10.371065; % Slab width
14 mu=1/sqrt(3); % Lattice speed in 1 dimension
15 N=10000; % Number of nodes
16 x=linspace(0,L,N); % Discretized width
17 dx=(x(2)-x(1)); % Node spacing
18 w=0.5; % Weight factors
19 S2(1:N)=10; % Source term
20 f1(1:N)=1; % Flux in the positive direction
21 f2(1:N)=1; % Flux in the negative direction
22 e1=1E-5; % Tolerance for Keff
23 e2=1E-5; % Tolerance for the source
24 err1=1; % Error for Keff
25 err2=1; % Error for the source
26 K1=0.001; % First Keff estimate
27 K2=1; % Second Keff estimate
28
29 while (err1>e1 || err2>e2)
30 % BOUNDARY CONDITIONS
31 f1(1)=0; % Vacuum conditions
32 f2(N)=0; % Vacuum conditions
33
34 % Store the previous source term
35 S=S2;
36
37 % COLLISION
38 f1=f1+dx/mu.*(w*(Sigma_s+nu*Sigma_f/K1).*(f1+f2)-Sigma_t.*f1);
39 f2=f2+dx/mu.*(w*(Sigma_s+nu*Sigma_f/K1).*(f1+f2)-Sigma_t.*f2);
40
41 % STREAMING
42 f1(2:N)=f1(1:N-1);
43 f2(1:N-1)=f2(2:N);
44
45 % CONVERGENCE
46 S2=nu*Sigma_f.*(f1+f2);
47 err2=max(abs((S2-S)./S2));
48 K2=K1*(sum(S2)/sum(S));
49 err1=abs((K2-K1)/K2);
50 K1=K2;
51 end
52 phi=f1+f2;
53
54 figure; hold on
55 plot(x,phi./phi(1))
```

Listing A.3: Matlab criticality code.

A.3 4 Region Critical Reactor

In Ch. 4 criticality is reported for a 4 region monoenergetic reactor using neutron diffusion theory as described in 4.5.2. A more detailed explanation of the diffusion theory solution for this problem is presented in this section for added clarity.

Table A.1: *One-group macroscopic cross sections for the 4 region reactor*

Material	ν	Σ_f (cm ⁻¹)	Σ_s (cm ⁻¹)	Σ_t (cm ⁻¹)
²³⁵ U	2.50	0.06922744	0.328042000	0.407407000
Fe	0.00	0.00000000	0.232094880	0.232560000
Na	0.00	0.00000000	0.086368032	0.086368032

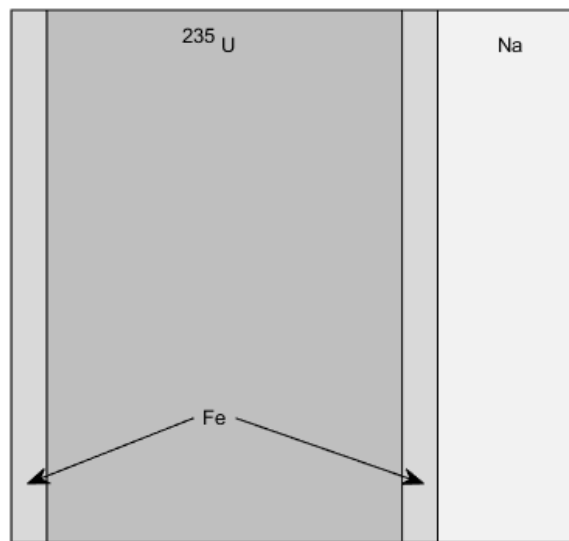


Figure A.3: *Slab geometry for the non-symmetric monoenergetic 4 region reactor with cladding and a moderator*

In this problem the reactor configuration is a uranium core surrounded on both sides by an iron cladding with a sodium reflector on the outside of only one side of the cladding, as shown in Fig. A.3. Let each region be denoted by subscripts 1-4 and introduce a buckling

term $B = \sqrt{\frac{\chi\nu\Sigma_f/K - \Sigma_a}{D}}$ in the core and $B = \sqrt{\frac{\Sigma_a}{D}}$ outside the core. Now the governing equations are given by

$$\frac{d^2\phi}{dx^2} = \begin{cases} -B^2\phi & \text{in the core} \\ B^2\phi & \text{otherwise} \end{cases} \quad (\text{A.1})$$

For the material cross sections, listed in Tab. A.1, it can be seen that $B = 0$ for the reflector region. This implies that the current, or first derivative of the flux, is constant in this region. With this information assumed flux profiles that satisfy Eq. A.1 in each region can be expressed as

$$\phi(x) = \begin{cases} A_1 \cosh(B_1x) + C_1 \sinh(B_1x) & \text{Left Fe cladding} \\ A_2 \cos(B_2x) + C_2 \sin(B_2x) & \text{U core} \\ A_3 \cosh(B_3x) + C_3 \sinh(B_3x) & \text{Right Fe cladding} \\ A_4x + C_4 & \text{Na reflector} \end{cases} \quad (\text{A.2})$$

There are 9 unknown parameters: the A_i and C_i coefficients and the criticality coefficient, K . A system of equations can be derived using boundary conditions as discussed in 4.5.2 and interface conditions such as

$$\phi_1(i) = \phi_2(i) \quad \text{and} \quad D_1 \frac{d\phi_1}{dx} \Big|_i = D_2 \frac{d\phi_2}{dx} \Big|_i \quad \text{for } i \in \text{interface} \quad (\text{A.3})$$

Denoting the interface locations as x_0 through x_4 the system of equations for the reactor

can be written as

$$\begin{aligned}
A_1 \cosh(B_1 x_0) + C_1 \sinh(B_1 x_0) &= 0 \\
A_1 \cosh(B_1 x_1) + C_1 \sinh(B_1 x_1) &= A_2 \cos(B_2 x_1) + C_2 \sin(B_2 x_1) \\
A_2 \cos(B_2 x_2) + C_2 \sin(B_2 x_2) &= A_3 \cosh(B_3 x_2) + C_3 \sinh(B_3 x_2) \\
A_3 \cosh(B_3 x_3) + C_3 \sinh(B_3 x_3) &= A_4 x_3 + C_4 \\
A_1 B_1 D_1 \sinh(B_1 x_1) + C_1 B_1 D_1 \cosh(B_1 x_1) &= -A_2 B_2 D_2 \sin(B_2 x_1) + C_2 B_2 D_2 \cos(B_2 x_1) \\
-A_2 B_2 D_2 \sin(B_2 x_2) + C_2 B_2 D_2 \cos(B_2 x_2) &= A_3 B_3 D_3 \sinh(B_3 x_2) + C_3 B_3 D_3 \cosh(B_3 x_2) \\
A_3 B_3 D_3 \sinh(B_3 x_3) + C_3 B_3 D_3 \cosh(B_3 x_3) &= A_4 D_4 \\
A_4 x_4 + C_4 &= 0
\end{aligned} \tag{A.4}$$

or in matrix form

$$\begin{bmatrix}
\cosh(B_1 x_0) & \sinh(B_1 x_0) & 0 & 0 & 0 & 0 & 0 & 0 \\
\cosh(B_1 x_1) & \sinh(B_1 x_1) & -\cos(B_2 x_1) & -\sin(B_2 x_1) & 0 & 0 & 0 & 0 \\
0 & 0 & \cos(B_2 x_2) & \sin(B_2 x_2) & -\cosh(B_3 x_2) & -\sinh(B_3 x_2) & 0 & 0 \\
0 & 0 & 0 & 0 & \cosh(B_3 x_3) & \sinh(B_3 x_3) & -x_3 & -1 \\
B_1 D_1 \sinh(B_1 x_1) & B_1 D_1 \cosh(B_1 x_1) & B_2 D_2 \sin(B_2 x_1) & -B_2 D_2 \cos(B_2 x_1) & 0 & 0 & 0 & 0 \\
0 & 0 & -B_2 D_2 \sin(B_2 x_2) & B_2 D_2 \cos(B_2 x_2) & -B_3 D_3 \sinh(B_3 x_2) & -B_3 D_3 \cosh(B_3 x_2) & 0 & 0 \\
0 & 0 & 0 & 0 & B_3 D_3 \sinh(B_3 x_3) & B_3 D_3 \cosh(B_3 x_3) & -D_4 & 0 \\
0 & 0 & 0 & 0 & 0 & 0 & x_5 & 1
\end{bmatrix}
\begin{bmatrix}
A_1 \\
C_1 \\
A_2 \\
C_2 \\
A_3 \\
C_3 \\
A_4 \\
C_4
\end{bmatrix}
= 0 \quad (\text{A.5})$$

The non-trivial solution requires the determinant of this matrix to be equal to zero. K is found by solving the resulting transcendental equation after setting the determinant equal to zero. Once K is known the resulting normalized flux profile can be obtained by taking $A_1 = 1$ and solving for the remaining coefficients.